

Differential exhumation of the Eastern Cordillera in the Central Andes: Evidence for south-verging backthrusting (Abancay Deflection, Peru)

Benjamin Gilles Gérard¹, Xavier Robert², Laurence Audin³, Pierre Valla¹, Matthias Bernet⁴, and Cecile Gautheron⁵

¹Université Grenoble Alpes

²ISTerre

³Isterre

⁴Universite Grenoble Alpes

⁵Université Paris Saclay

November 21, 2022

Abstract

Located at the northern tip of the Altiplano, the Abancay Deflection marks abruptly the latitudinal segmentation of the Central Andes spreading over the Altiplano to the south and the Eastern Cordillera northward. The striking contrast in terms of morphology between the low-relief Altiplano and the high-jagged Eastern Cordillera makes this area a privileged place to determine spatio-temporal variations in surface and/or rock uplift and discuss the latest phase of the formation of the Central Andes. Here, we aim to quantify exhumation and uplift patterns in the Abancay Deflection since 40 Ma, and present new apatite (U-Th)/He and fission-track data from five altitudinal profiles and additional individual samples. Age-Elevation relationships and thermal modeling both evidence that the Abancay Deflection experienced a moderate, spatially-uniform and steady exhumation at 0.2 ± 0.1 km/m.y. between 40 Ma and ~ 5 Ma implying common large-scale exhumation mechanisms. From ~ 5 Ma, while the northern part of the Eastern Cordillera and the Altiplano registered similar ongoing slow exhumation, the southern part of the Eastern Cordillera experienced one order-of-magnitude of exhumation acceleration (1.2 ± 0.4 km/m.y). This differential exhumation since ~ 5 Ma implies active tectonics, river capture and incision affecting the southern Eastern Cordillera. 3D thermo-kinematic modeling favors a tectonic decoupling between the Altiplano and the Eastern Cordillera through backthrusting activity of the Apurimac fault. We speculate that the Abancay Deflection, with its “bull’s-eye” structure and significant exhumation rate since 5 Ma, may represent an Andean proto-syntaxis, similar to the syntaxes described in the Himalaya or Alaska.

1 **Differential exhumation of the Eastern Cordillera in the Central Andes:**
2 **Evidence for south-verging backthrusting (Abancay Deflection, Peru)**

3
4 **Benjamin Gérard¹, Xavier Robert¹, Laurence Audin¹, Pierre G. Valla^{1,2}, Matthias**
5 **Bernet¹, Cécile Gautheron³**

6
7 ¹Univ. Grenoble Alpes, Univ. Savoie Mont Blanc, CNRS, IRD, IFSTTAR, ISTerre, 38000
8 Grenoble, France

9 ²Institut of Geological Sciences, University of Bern, Baltzerstrasse 3, 3012 Bern, Switzerland

10 ³ Université Paris-Saclay, CNRS, GEOPS, 91405, Orsay, France

11
12 Corresponding author: Benjamin Gérard (benjamin.gerard.alpes@gmail.com)

13
14 **Key Points:**

- 15 • Thermochronological data quantifying the tectonic history of the undocumented
16 northern edge of the Peruvian Altiplano (Abancay Deflection)
- 17 • 3-D Thermo-kinematic models unravel the evolution of the Eastern Cordillera & the
18 Altiplano
- 19 • Steady and uniform exhumation between 40 and 5 Ma, followed by tectonically-
20 driven tilting of the Eastern Cordillera

26 **Abstract**

27 Located at the northern tip of the Altiplano, the Abancay Deflection marks abruptly
28 the latitudinal segmentation of the Central Andes spreading over the Altiplano to the south
29 and the Eastern Cordillera northward. The striking contrast in terms of morphology between
30 the low-relief Altiplano and the high-jagged Eastern Cordillera makes this area a privileged
31 place to determine spatio-temporal variations in surface and/or rock uplift and discuss the
32 latest phase of the formation of the Central Andes. Here, we aim to quantify exhumation and
33 uplift patterns in the Abancay Deflection since 40 Ma, and present new apatite (U-Th)/He
34 and fission-track data from five altitudinal profiles and additional individual samples. Age-
35 Elevation relationships and thermal modeling both evidence that the Abancay Deflection
36 experienced a moderate, spatially-uniform and steady exhumation at 0.2 ± 0.1 km/m.y.
37 between 40 Ma and ~5 Ma implying common large-scale exhumation mechanisms. From ~5
38 Ma, while the northern part of the Eastern Cordillera and the Altiplano registered similar
39 ongoing slow exhumation, the southern part of the Eastern Cordillera experienced one order-
40 of-magnitude of exhumation acceleration (1.2 ± 0.4 km/m.y). This differential exhumation
41 since ~5 Ma implies active tectonics, river capture and incision affecting the southern Eastern
42 Cordillera. 3D thermo-kinematic modeling favors a tectonic decoupling between the
43 Altiplano and the Eastern Cordillera through backthrusting activity of the Apurimac fault. We
44 speculate that the Abancay Deflection, with its “bulls-eye” structure and significant
45 exhumation rate since 5 Ma, may represent an Andean proto-syntaxis, similar to the syntaxes
46 described in the Himalaya or Alaska.

47

48 **Keywords:** Central Andes, Abancay Deflection, Thermochronology, Differential
49 exhumation, Tectonic decoupling, Apurimac fault system

50

51 **1 Introduction**

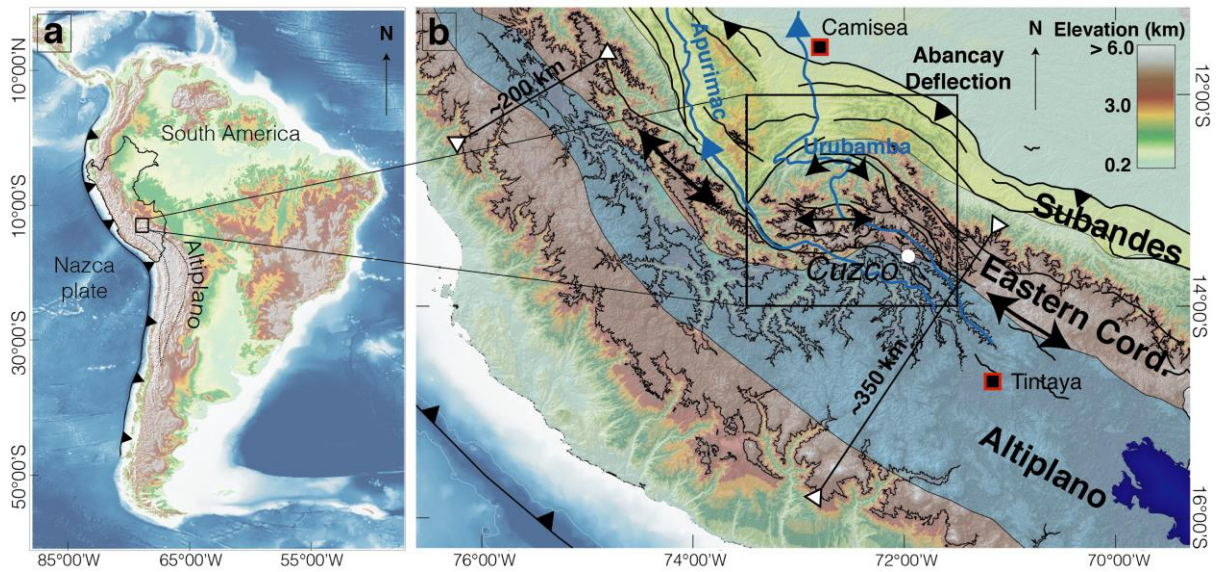
52 The Central Andes contain the second-highest and widest plateau on Earth: the
53 Altiplano. Andean topography building started during the Cretaceous (~120-110 Ma; Jaillard
54 & Soler, 1996). Tectonic, climatic and erosional interactions affecting the Altiplano and its
55 eastward border, the Eastern Cordillera (**Figure 1**), have been extensively studied in the
56 southern Central Andes (Bolivia, Argentina; Strecker et al., 2007). The northern edge of the
57 Altiplano, namely the Abancay Deflection (southern Peru; Marocco, 1971; Dalmayrac et al.,
58 1980; **Gérard et al., submitted**), however, has been poorly documented, although its relief and
59 structural organization reveals spectacular specificities with deflected drainage basins and
60 rivers, and deeply-incised landforms. The Abancay Deflection occupies a part of the
61 Altiplano to the south and the Eastern Cordillera northward (**Figures 1 & 2**), and is limited to
62 the north by the Subandes. Morphologically, the Altiplano and the Eastern Cordillera
63 acquired their respective modern mean elevation of ~4 km and ~4.5 km before 5 Ma (Sundell
64 et al., 2019).

65 Mechanisms for exhumation of the Bolivian and southern Peru Eastern Cordillera are
66 debated and imply either east-verging thrusting along a ramp connected to the Subandean
67 zone (Gotberg et al., 2010; Rak et al., 2017), or reactivation of inherited faults as west-
68 verging backthrusts (Perez et al., 2016), both with subsequent erosion of the built topography.
69 In Bolivia, the Eastern Cordillera experienced exhumation between 50 and 15 Ma with
70 transfer of tectonic deformation to the Subandean zone at ~15 Ma (Barnes et al., 2012). From
71 thermochronological records, the northern Altiplano has been suggested to experience a
72 steady exhumation of ~0.2 km/m.y. between ~40 and ~15 Ma (Ruiz et al., 2009). The limited
73 records before 38 Ma and after 14 Ma for this area, however, prevents from deciphering
74 and/or speculating between different surface-uplift scenarios such as slow and continuous
75 surface uplift associated with (lower) crustal deformation since 40 Ma (Barnes & Ehlers,

76 2009; Husson & Sempere, 2003; Ouimet & Cook, 2010), versus potential surface-uplift
77 acceleration during the Miocene triggered by lithospheric delamination event(s) (Garzzone et
78 al., 2017). The high-relief Eastern Cordillera seems to register a more recent and complex
79 exhumation history (< 5 Ma) with both incision and regressive erosion (Lease and Ehlers,
80 2013; Gérard et al. submitted).

81 Regarding the climate imprint over the Eastern Cordillera, major canyon carving is
82 supposedly related to Pliocene global climate cooling (Lease & Ehlers, 2013). Nonetheless,
83 increased orographic precipitation in such a rising orogen (Insel et al., 2010), could explain
84 also canyon incision events earlier than the Pliocene (Poulsen et al., 2010). Even though the
85 timing of surface uplift and mechanisms of exhumation are debated, there is a clear contrast
86 and decoupling in terms of vertical motion between the Altiplano, the Eastern Cordillera and
87 the Subandes. Our aim is to provide further quantitative constraints to unravel the
88 mechanisms responsible for the Abancay Deflection exhumation and uplift since 40 Ma.

89 The deeply-incised Abancay Deflection is the ideal target to unravel the long-term
90 evolution of the northern edge of the Altiplano (Figure 1). Here we present new apatite (U-
91 Th)/He (AHe) and fission-track (AFT) data, targeting Permo-Triassic (Mišković et al., 2009)
92 and Paleogene (Carlier et al., 1996; Mamani et al., 2010) plutonic bedrocks along high-relief
93 valleys. We have interpreted these thermochronological data using Age-Elevation
94 Relationships (AER; Glotzbach et al., 2011), thermal (2D; QTQt; Gallagher, 2012) and
95 thermo-kinematic (3D; Pecube; Braun, 2003; Braun et al., 2012) modeling to determine the
96 late-Eocene to modern exhumation history of the Abancay Deflection and discuss potential
97 exhumation mechanisms.



98

99

Figure 1. Abancay Deflection location. a) Location within South America of the study area at the northern tip of the Altiplano in Peru. b) Zoom-in on the Abancay Deflection area (black square in panel a). Double black arrows highlight the topography elongation axis. Note the pronounced incision within the study area through the iso-elevation line (black) at 3.8 km elevation via the Urubamba and Apurimac rivers (blue) canyons. Black thin lines framed by white triangles highlight the latitudinal range width variation with the Abancay Deflection as the transition zone between the northern narrow Peruvian Andes and the southern wide Bolivian Orocline. Black squares with red borders are the places where thermal parameters were measured.

108

109

110

111

112

113

114

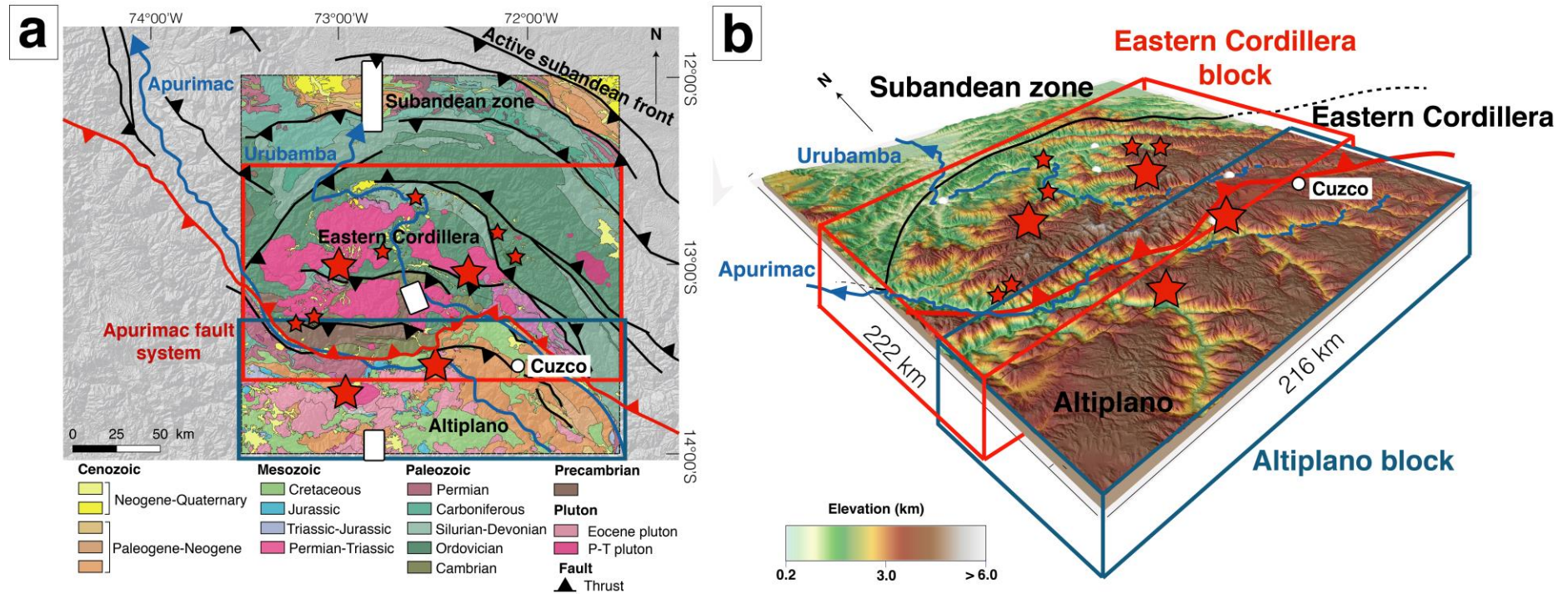
115

116 **2 Geological setting**

117 The Abancay Deflection occupies the morpho-tectonic regions of the Altiplano to the
118 south and the Eastern Cordillera to the north, separated by the crustal-scale Apurimac fault
119 system (Figure 2). This fault system seems to affect the study area since at least the Permian
120 (by a transform fault in an extensional context; Sempere et al., 2002). Eocene plutons (50-30
121 Ma; Mamani et al., 2010) emplaced into Meso-Cenozoic sediments (Carlier et al., 1996) crop
122 out in the Altiplano whereas Permo-Triassic batholiths are dominant in the Eastern Cordillera
123 and intrude into Paleozoic rocks (Figure 2; Mišković et al., 2009). Thermal perturbation
124 linked to magmatic arc activity ceased after ~30 Ma and the ultimate local volcanic events
125 (from 7 to 0.5 Ma; Bonhomme et al., 1988) focused along the Apurimac fault system.
126 Inherited deflected faults and arched-captured rivers characterize the Abancay Deflection on
127 the northern edge of the Altiplano that records high-magnitude counterclockwise tectonic
128 rotation since 40 Ma (Roperch et al., 2006) in a Bolivian Orocline bending context (Müller et
129 al., 2002).

130 The Subandean zone and the Altiplano are documented as tectonically active
131 respectively in shortening and extensional context (Figure 3) since ~14 Ma in the Subandes
132 (Espurt et al., 2011; Gautheron et al., 2013) and since ~5 Ma in the Altiplano (Cabrera et al.,
133 1991). In between, the Eastern Cordillera limited southward by the Apurimac fault system
134 presents nowadays a non-negligible low-magnitude crustal seismicity (Figure 3a), however,
135 too low to determine a tectonic behavior (Figure 3b). Preliminary thermochronological
136 investigation into the core of the Eastern Cordillera (Machu Picchu), nonetheless, favors a
137 post ~4 Ma acceleration of incision-driven exhumation but this inference is restricted to the
138 local area of Machu Picchu and cannot be extended yet for the entire Abancay Deflection
139 (Gérard et al. Submitted). Also, this previous study can neither evidence nor discard potential
140 tectonic-driven exhumation. The observed seismicity for the Apurimac fault system area

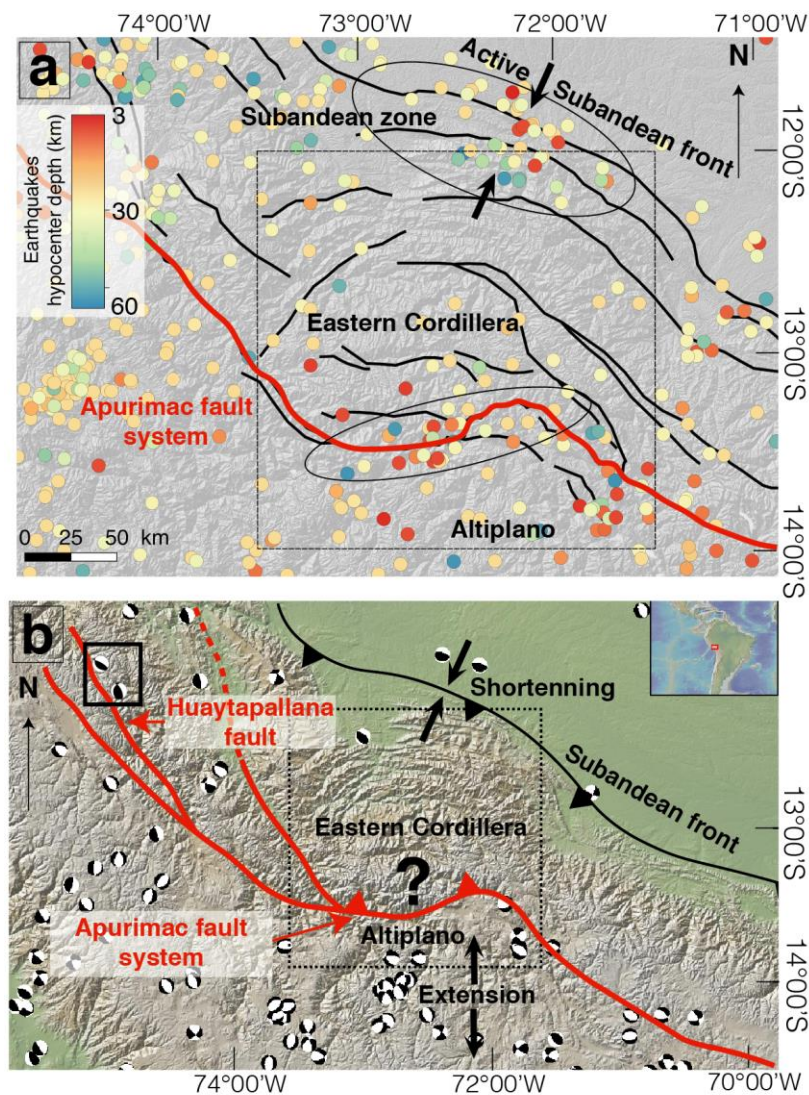
141 could be linked and/or connected with either Subandean flat-ramp thrust systems or
142 undocumented active internal backthrusts, or even normal faulting as in the Altiplano.
143 Though, potential tectonic drivers responsible for the building of the Abancay Deflection and
144 particularly for the Eastern Cordillera part remain unknown. Quantitative thermochronology
145 and modeling represent the ideal tools to explore exhumation pattern for the whole area
146 addressing exhumation mechanisms.



147

148 **Figure 2.** Geology and morphology of the Abancay Deflection. a) Geological map of the study area. The crustal scale Apurimac fault system
 149 marks the tectonic limit between the Altiplano and the Eastern Cordillera. (INGEMMET geological map database - 1:100,000). White rectangles
 150 refer to previous thermochronological studies; references are provided in the method and results sections. b) 3D DEM of the Abancay
 151 Deflection. For both panels, red stars are the thermochronological sample location (vertical profiles and individual data; this study). 2D colored
 152 rectangles (a) and corresponding 3D views (b) are crustal block locations processed with 3D thermo-kinematics modeling using Pecube for the
 153 Altiplano (blue) and the Eastern Cordillera (red) blocks.

154



155

156 **Figure 3.** Crustal seismic map of the Abancay Deflection (Dashed squares; hypocenters < 60
 157 km; $M_w > 2$). a) Mapped earthquakes come from the USGS, IGP and ISC databases. Regions
 158 included into black ellipses emphasize positive anomalous cluster of seismicity. Black lines
 159 represent the major thrusts of the studied area. b) Moment tensors (CMT) for earthquakes
 160 (1969-2019) for the Abancay Deflection region (Dziewonski et al., 1981; Ekström et al.,
 161 2012). Focal mechanisms (transpressional) for the two 1969 Huaytapallana events are framed
 162 by the black rectangle (Dorbath et al., 1990; Suarez et al., 1983). There are no CMT data for
 163 $M_w < 5.5$ earthquakes. Tectonic shortening characterizes the Subandean front whereas
 164 extensional mechanisms affect the Altiplano.

165 **3 Methods**

166 AHe and AFT thermochronology are based on He and fission track production during
167 alpha decay of U, Th and Sm and fission decay of U respectively with associated He and
168 fission tracks accumulation within apatite crystals. Using a rate of He diffusion rate out of the
169 crystals or fission track annealing with temperature, those methods can be used to record the
170 thermal evolution of the upper crust, given their thermal sensitivity ranges spanning from
171 ~80-40°C (Ault et al., 2019) and ~75-125°C (Reiners & Brandon, 2006) respectively for
172 active mountain ranges, depending on cooling rate and/or holding time within the respective
173 partial retention/annealing zones. Thus, low-temperature thermochronology records the
174 thermal evolution of the upper crust (< 5 km) and is a key to decipher between different
175 exhumation mechanisms through time-evolving rock uplift and landscape evolution (Ault et
176 al., 2019; Reiners & Shuster, 2009). Quantitative interpretation with three different types of
177 models (*i.e.* geometric, thermal and thermo-kinematic, sections 3.2-3.4) with different
178 degrees of complexity makes it possible to test model robustness and propose highly
179 consistent scenarios for the exhumation of the Abancay Deflection.

180

181 **3.1 Low-temperature thermochronological data**

182 We collected 33 samples from magmatic bedrock of five high-altitude profiles
183 (Ocobamba, Lucma, Incahuasi, Abancay and Limatambo) and 4 individual samples collected
184 across the Abancay Deflection to get an optimal coverage of the study area (Figures 2 & 4;
185 Table 1). Granitic samples were crushed and sieved at the Géode laboratory (Lyon, France)
186 to extract the 100-160 µm fractions. Apatite crystals were concentrated using standard
187 magnetic and heavy-liquid separation techniques at the GeoThermoChronology (GTC)
188 platform within the ISTerre laboratory (Université Grenoble Alpes, France).

189 For AHe dating single euhedral apatite crystals were carefully selected under a
190 binocular microscope to identify minerals without fractures and/or inclusions that would
191 skew the AHe age (diffusion artifacts and/or additional ^4He sources; Farley, 2002). We
192 determined the individual grain geometry and calculated the alpha-ejection correction factor
193 using the Qt_FT program (Gautheron and Tassan-Got, 2010; Ketcham et al., 2011).
194 Individual apatites were encapsulated in platinum tubes allowing apatite heating and
195 manipulation. Each apatite in its platinum tube was then heated under ultra-vacuum
196 conditions at high temperature ($1050\pm 50^\circ\text{C}$ using an infrared diode laser) twice for 5 min at
197 GEOPS laboratory (Université Paris Saclay, France). The ^4He gas was mixed with a known
198 amount of ^3He , purified and the gas was analyzed using a Prisma Quadrupole. The ^4He
199 content was determined by isotopic dilution. Subsequently, apatite crystals were dissolved in
200 100 μl of HNO_3 5N solution containing known amount of ^{235}U , ^{230}Th , ^{149}Sm and ^{42}Ca . The
201 solution was heated at 70°C during 3 h and after a cooling time, 900 μl of distilled water was
202 added. The final solution was analyzed using an ELEMENT XR ICP-MS and the ^{238}U , ^{230}Th
203 and ^{147}Sm concentrations and apatite weight (using the Ca content) were determined
204 following the methodology proposed by Evans et al. (2005). Durango apatite crystals were
205 also analyzed during the same period to ensure the data quality. The one-sigma error on each
206 AHe age amounts to 8%, reflecting the analytical error and the uncertainty on the FT ejection
207 factor correction. More details about the analytical procedure can be found in Recanati et al.
208 (2017).

209 For AFT dating at the GTC laboratory (ISTerre, Grenoble, France), apatites were
210 mounted in epoxy resin, polished, and etched for 20 s at 21°C using a 5.5 M HNO_3 solution
211 to reveal spontaneous fission tracks. Using the external detector method, all samples were
212 irradiated together with age standards at IRMM540R dosimeter glasses at the FRM II reactor
213 (Munich, Germany). Tracks were counted and horizontally confined track lengths were

214 measured at ISTerre. We used the BINOMFIT program (Ehlers et al., 2005) to calculate the
215 AFT central ages.

216

217 **3.2 Age-Elevation Relationships (AER)**

218 For AER modeling, single- or multi-tier age-elevation relationships (AER) to the AFT
219 and AHe data from altitudinal profile data were fit using a Bayesian approach to obtain a
220 first-order estimate of apparent exhumation rates and evidence potential break-in-slope
221 through time by minimization of the Bayesian Information Criterion (BIC; Glotzbach et al.,
222 2011; Schwarz, 1978). This process gives first-order constraints regarding exhumation rates
223 and potential exhumation changes through time for each vertical profile. These apparent
224 exhumation rates are, nonetheless, free from any consideration regarding the inter-sample
225 AHe/AFT kinetic variability, the thermal crustal regime, the relief evolution and the isostasy
226 assuming a quasi-vertical profile (Stüwe et al., 1994). These modeling biases will be taken
227 into account with 2D thermal and 3D thermo-kinematic modeling described hereafter.

228

229 **3.3 Time-temperature modeling (QTQt)**

230 Time-temperature modeling with QTQt (Bayesian transdimensional and MCMC
231 sampling; Gallagher, 2012) gives strong constrains regarding thermal histories for individual
232 samples, with the possibility to combine and process multi-samples from high-altitudinal
233 profiles. We processed 300,000 iterations for both individual sample and vertical profiles
234 exploring T-t paths with their respective likelihood allowing extracting best-fitting thermal
235 histories. We used the implemented annealing model of Ketcham et al. (2007) and the
236 radiation damage model of Gautheron et al. (2009) for AFT and AHe data respectively. We
237 allowed the geothermal gradient to vary over time for values spreading over 10 and 40°C/km
238 commonly associated for the non-volcanic Central Andes (Barnes et al., 2008). The timespan

239 explored starts twice as the older thermochronological age for each profile to eliminate any
240 potential temporal bias.

241 Assessing the geothermal gradient is a crucial point for exhumation rate computation,
242 and the Abancay Deflection is totally devoid of direct measurements. We computed a
243 geothermal gradient according to the nearest thermal parameter measurements and/or
244 accepted values for these parameters. According to heat flow and thermal conductivity
245 measurements in the Tintaya mine (Figure 1b; Henry & Pollack, 1988), crustal average heat
246 production ($\sim 0.9 \mu\text{W}/\text{m}^3$; Springer, 1999), thermal diffusivity for a granitic bedrock (~ 40
247 $\text{km}^2/\text{m.y.}$; Arndt et al., 1997; Whittington et al., 2009) and a $\sim 25^\circ\text{C}$ surface temperature
248 (Gonfiantini et al., 2001) we obtained a geothermal gradient of $18 \pm 4^\circ\text{C}/\text{km}$ (Text S1). This
249 computed value is consistent with direct measurements inferred from the Camisea area
250 ($\sim 17^\circ\text{C}/\text{km}$; Figure 1b; Espurt et al., 2011) and the Tintaya mine ($\sim 14^\circ\text{C}/\text{km}$; Henry &
251 Pollack, 1988). Moreover, this value overlaps with compiled geothermal gradient values for
252 the Eastern Cordillera (Bolivia; $26 \pm 8^\circ\text{C}/\text{km}$; Barnes et al., 2008).

253 We thus convert cooling histories derived from QTQt expected models into
254 exhumation rates, using an assumed constant and spatially-uniform geothermal gradient of
255 $18 \pm 4^\circ\text{C}/\text{km}$. Magmatic arc activity of the Abancay Deflection and its potential thermal
256 perturbation ceased after ~ 30 Ma (Mamani et al., 2010) and there is no evidence for posterior
257 reheating. For the surface, we implemented a lapse rate (temperature loss with altitude
258 increasing) of $\sim 6^\circ\text{C}/\text{km}$ according to Gonfiantini et al. (2001) for the eastern flank of the
259 inter-tropical Andes. Parameters used for QTQt data inversion are displayed in the Table S1.

260

261 **3.4 Thermo-kinematic modeling (Pecube)**

262 **3.4.1 Pecube**

263 Pecube is the only option, and presents the considerable advantage to simultaneously
264 test numerous tectonic or incision scenarios in 3D, computing thermal histories and to
265 confront numerical predictions to observed thermochronological data along altitudinal
266 profiles or for local data. Pecube computes thermal histories for rock particles at depth in
267 exhumation or burial contexts, taking into account landscape evolution (topography, relief),
268 the thermal regime of the crust, the tectonic settings (faults, uplift or subsidence) and isostasy
269 (Braun, 2003; Braun et al., 2012). Solving the 3D heat transfer equation in the crust, the
270 thermo-kinematic program Pecube v4.2 (Braun, 2003; Braun et al., 2012) predicts the spatial
271 distribution of thermochronological ages for specific samples considering exhumation
272 through lateral and vertical rock kinetics and relief evolution. We used Pecube in inverse
273 mode (Neighborhood Algorithm - NA; Sambridge, 1999a;b) to determine optimal value
274 ranges for tested parameters by minimizing the misfit function between predictions and
275 observations (Text S2).

276

277 **3.4.2 Input data and fixed parameters**

278 We processed thermochronological data including AFT and AHe thermochronometric
279 systems. We used 33 AHe ages (AHe mean grain ages, 28 new data and 5 from Gérard et al.,
280 submitted) and 42 AFT ages (AFT central ages, 32 new data, 2 from Kennan (2008) and 8
281 from Ruiz et al. (2009)). We implemented into Pecube present-day topography extracted
282 from the global elevation database GTOPO30 (Figure 5). He diffusion coefficient and AFT
283 annealing model from Farley (2000) and Ketcham et al. (1999) respectively have been
284 implemented into Pecube. For AHe data, we chose the Farley (2000) model for He diffusion
285 as it presents mean values for the diffusion coefficient for low-damaged apatites. In our case,
286 as exhumation histories are simple without identified reheating, damage influence plays a
287 minor role in the diffusion process. This model is identical to the Gautheron et al. (2009)

288 diffusion model in such a case. It is not possible with Pecube to reproduce the AHe age
289 dispersion between crystals due to damage impact on He diffusion (Gautheron et al., 2009;
290 Shuster et al., 2006). So, we here decided to implement the average ages and standard
291 deviation errors (Table S2). Regarding the AFT data, we also implemented track-length
292 measurements when available. Finally, Pecube model outcomes were also directly compared
293 to T-t paths derived from QTQt modeling.

294 In order to optimize computation time, we divided the Abancay Deflection into two
295 crustal blocks (Altiplano vs. Eastern Cordillera; Figure 2) that we modeled independently,
296 except for the exploration of the model thermal diffusivity vs. the basal temperature where
297 the Altiplano and the Eastern Cordillera were investigated together. Each of these crustal
298 blocks represents the natural tectono-morphic boundary of the Abancay Deflection. The
299 timespan explored starts at 50 Ma for all the simulations to eliminate any potential temporal
300 bias. We subsequently divided the explored timespan into six time slices: 50, 25, 15, 10, 5
301 and 0 Ma. For each time boundary, we fit the modeled mean paleo-elevation according to
302 Sundell et al. (2019). We do not have, however, any information regarding the relief
303 evolution of the Abancay Deflection that sits in a remote location never sampled before nor
304 any proxy for incision (Text S4). Finally, for exhumation rate quantification from
305 thermochronological data, we fixed the crustal thermal and rheological parameters in space
306 and time (Figure 5; Table S3). For these parameters, we finally explored the basal
307 temperature of the crustal block and the thermal diffusivity to test our chosen geothermal
308 gradient (Table S4).

309

310 **3.4.3 Neighborhood Algorithm inversions and explored parameters**

311 We used Pecube in inverse mode to quantitatively constrain parameter values
312 (tectono-morphic scenarios) that best reproduce the input thermochronological data. We

313 extracted the best-fitting parameter values for each inversion computing probability density
314 functions (Sambridge, 1999a;b). When the inversion clearly converges toward a unique
315 parameter solution (one peak for the probability density function), we extracted the parameter
316 value applying the 2σ standard deviation. We consequently used forward Pecube modeling to
317 present the best-fitting scenarios and data reproducibility using inversion-derived parameters
318 as input data ([Supporting Information](#)).

319 We first broadly explored the basal temperature and the thermal diffusivity to test our
320 geothermal gradient calculation ([Table S4](#)). Here, we investigated together the Altiplano and
321 the Eastern Cordillera crustal blocks. Because of computing time issues with the global
322 model, and as the Altiplano and the Eastern Cordillera present opposite morphologies (flat vs.
323 deeply incised; [Gérard et al., submitted](#)), and different exhumation trends according to local
324 studies (slow and continuous (Ruiz et al., 2009) vs. recent acceleration (Kennan, 2008;
325 [Gérard et al. submitted](#)), we explored these areas separately with the ultimate goal to unravel
326 the exhumation pattern. For the Altiplano model, we explored the basal crustal temperature
327 (proxy for the geothermal gradient; [Figure 5](#)), the exhumation history for the entire crustal
328 block ([Figure 5](#)), and landscape evolution through time (Topography offset and relief
329 amplification factor; [Figure S38](#)). For the Eastern Cordillera model, we explored the
330 exhumation history for the entire crustal block ([Figure 5](#)), relief and topographic evolution
331 ([Figure S38](#)), and the kinematics of the Apurimac fault system (fault dip, timing of initiation
332 and fault velocity; [Figure 5](#)). The detailed list of the explored Pecube parameters is available
333 in [Table S4](#).

Table 1. Sample locations and bedrock lithologies

Sample number	Latitude (°S)	Longitude (°W)	Elevation (m)	Lithology	Geologic unit	Pluton age
<u>Ocobamba profile*</u>						
AB-17-05	13.091198	72.26337	3903	Granite	Mesapelada pluton	Permian
AB-17-06	13.07867	72.27952	3696	Granite	Mesapelada pluton	Permian
AB-17-07	13.07128	72.2803	3447	Granite	Mesapelada pluton	Permian
AB-17-08	13.05875	72.28962	3190	Granite	Mesapelada pluton	Permian
AB-17-11	13.00978	72.3299	2450	Monzonite	Mesapelada pluton	Permian
<u>Individual data</u>						
AB-17-13	12.83221	72.14085	1638	Granite	Colca pluton	Permian
AB-17-15	12.9652	72.07252	2475	Granite	Colca pluton	Permian
AB-17-18	12.64752	72.55498	912	Granite	Quellotuno pluton	Triassic
AB-17-19	12.89585	72.74471	1362	Granite	Kiteni pluton	Triassic
<u>Lucma profile*</u>						
AB-17-21	13.04408	72.88454	2235	Granite	Kiteni pluton	Triassic
AB-17-22	13.04171	72.93961	3020	Granite	Kiteni pluton	Triassic

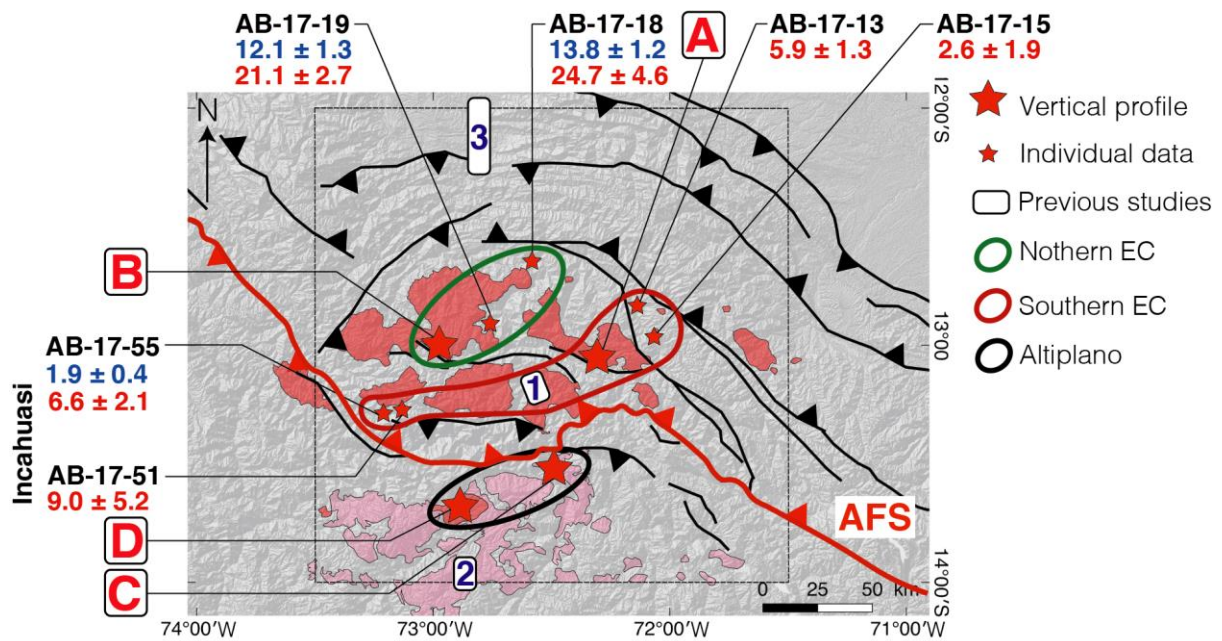
Sample number	Latitude (°S)	Longitude (°W)	Elevation (m)	Lithology	Geologic unit	Pluton age
AB-17-23	13.02889	72.9593	3678	Granite	Kiteni pluton	Triassic
AB-17-25	13.00124	72.9468	4050	Granite	Kiteni pluton	Triassic
AB-17-26	13.03244	72.9577	3589	Granite	Kiteni pluton	Triassic
AB-17-28	13.05984	72.9371	2609	Granite	Kiteni pluton	Triassic
<u>Limatambo profile*</u>						
AB-17-29	13.5299	72.43471	4056	Diorite	Cotabamba pluton	Paleogene
AB-17-30	13.53367	72.45849	3795	Diorite	Cotabamba pluton	Paleogene
AB-17-31	13.5419	72.4688	3581	Diorite	Cotabamba pluton	Paleogene
AB-17-32	13.52771	72.4671	3322	Diorite	Cotabamba pluton	Paleogene
AB-17-33	13.51888	72.47569	2966	Diorite	Cotabamba pluton	Paleogene
AB-17-34	13.50543	72.4702	2740	Diorite	Cotabamba pluton	Paleogene
AB-17-35	13.50373	72.47325	2586	Diorite	Cotabamba pluton	Paleogene
AB-17-36	13.49839	72.48075	2435	Diorite	Cotabamba pluton	Paleogene
<u>Abancay profile*</u>						
AB-17-37	13.67147	72.89801	2800	Monzonite	Abancay orthogneiss	Triassic

Sample number	Latitude (°S)	Longitude (°W)	Elevation (m)	Lithology	Geologic unit	Pluton age
AB-17-38	13.67129	72.90512	2573	Diorite	Abancay orthogneiss	Triassic
AB-17-39	13.6721	72.90939	2280	Gabbro	Abancay orthogneiss	Triassic
AB-17-40	13.68018	72.91482	1916	Granite	Abancay orthogneiss	Triassic
AB-17-41	13.68651	72.84196	4136	Granite	Abancay orthogneiss	Triassic
AB-17-42	13.67414	72.85007	3753	Granite	Abancay orthogneiss	Triassic
AB-17-43	13.66636	72.86651	3459	Granitic arena	Abancay orthogneiss	Triassic
AB-17-44	13.6792	72.88035	3209	Granitic arena	Abancay orthogneiss	Triassic
<u>Incahuasi profile*</u>						
AB-17-51	13.2918	73.15121	3434	Granite	Chucuito pluton	Devonian
AB-17-55	13.30613	73.21085	2455	Granite	Chucuito pluton	Devonian

Note: The Geologic unit and pluton age columns refer to the studies of Egeler & De Booy (1961), Lancelot et al. (1978), Mišković et al. (2009), Perello et al. (2003), Reitsma (2012) and the INGEMMET geological database.

* Profile names were given considering the main cities nearby the investigated area.

336



337

338 **Figure 4.** Sample locations of the new thermochronological ages within the Abancay

339 Deflection. Red and pink polygons are respectively Permo-Triassic and Eocene plutons.

340 Previous studies are: 1: Gérard et al. (submitted) and Kennan (2008); 2: Ruiz et al. (2009); 3:

341 Espurt et al. (2011) and Gautheron et al. (2013). Blue and red numbers below sample names

342 refer to AHe mean ages and AFT central ages for individual samples and the two-sampled-

343 point Incahuasi vertical profile. Red capital letters refer to the other sampled vertical profiles

344 (A: Ocobamba profile; B: Lucma profile; C: Limatambo profile & D: Abancay profile).

345 Profiles results are displayed in Figure 6. Green, red and black contours mark the latitudinal

346 segmentation of the Abancay Deflection defining three areas according to thermal histories

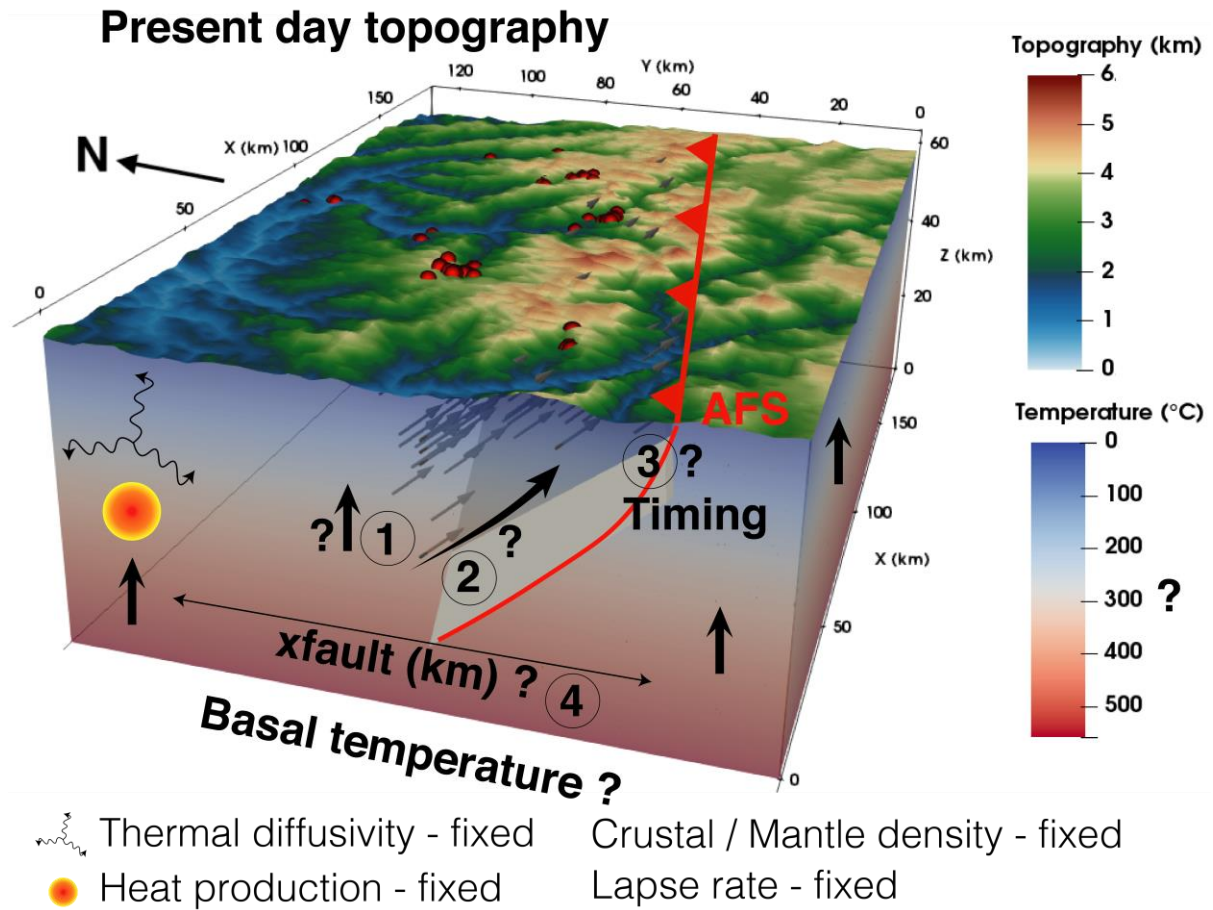
347 modeled with QTQt (*i.e.* Northern EC, Southern EC and Altiplano respectively). The black

348 dashed square frames the Abancay Deflection. AFT: Apurimac fault system; EC: Eastern

349 Cordillera.

350

351



352

353

354

355

356

357

358

359

360

Figure 5. Parameters implemented and/or explored in Pecube through time. Example for the Eastern Cordillera crustal block (see [Figure 2](#) for location). For the Altiplano block we only explored the crustal block exhumation (1). Red dots mark the location of the thermochronological data. Numbers and question marks refer to explored parameters. 1: Crustal block exhumation (km/Ma); 2: Fault velocity (km/Ma); 3: Timing of fault activation (Ma); 4: x fault (km), proxy for the fault geometry (fault dip). AFS: Apurimac fault system. Additional details are given in [Table S4](#) & [Figure S38](#).

361 **4 Results**

362 **4.1 New thermochronological ages and AERs**

363 For the entire Abancay Deflection area, the new 108 single-crystal AHe ages (from 28
364 samples) and the 27 AFT central ages range from 0.7 ± 0.1 to 35.8 ± 2.9 Ma and 2.6 ± 1.9 to
365 38.2 ± 4.4 Ma respectively, covering a temporal range from the late Eocene to the late
366 Pleistocene (Figure 4 & 6; Tables 2 and 3). Reproducibility of single-crystal AHe ages is
367 satisfactory with averaged dispersion $< 10\%$ for the whole dataset. For AFT central ages, all
368 samples passed the χ^2 test ($> 5\%$; Table 3; Figures S1 to S27), meaning that we can consider
369 single-age populations for each sample (Green, 1981). Thermochronological ages ranging up
370 to ~ 40 Ma are characteristic of the northern Eastern Cordillera and the Altiplano, as shown
371 for the Lucma, Abancay and Limatambo altitudinal profiles and individual data (AB-17-19
372 and AB-17-18; Figure 4 & 6). The southern Eastern Cordillera presents much younger
373 thermochronological ages, all < 10 Ma (Ocobamba and Incahuasi profiles, AB-17-13 and AB-
374 17-15; Figure 4 & 6).

375 For all altitudinal profiles, both AHe and AFT ages best fit a single AER, but they
376 reveal different rates and timing of exhumation (Figure 6). The Lucma profile presents an
377 apparent exhumation rate of ~ 0.1 km/m.y. between 40 to 0 Ma, while the Abancay and
378 Limatambo profiles give apparent exhumation rates between 0.1 to 0.2 km/m.y. with a
379 possible increase in exhumation since 10-15 Ma. The Ocobamba profile presents much
380 higher apparent exhumation rates for the last 6 Ma, with $0.5_{-0.1}^{+0.2}$ km/m.y. for AHe and $0.9_{-0.4}^{+3.7}$
381 km/m.y. for AFT. These exhumation rates values correspond to the lowest computed BIC and
382 consequently the best-fitting solutions according to the Bayesian approach (Glotzbach et al.,
383 2011).

384

385 **4.2 Numerical thermo(-kinematic) modeling**

386 Modeled Time-temperature paths with QTQt show for the entire study area a
387 moderate and continuous cooling history with a cooling rate of $\sim 2.5^{\circ}\text{C}/\text{m.y.}$ between 40 and
388 ~ 5 Ma (Figure 7). Even if cooling trends are relatively similar for the northern Eastern
389 Cordillera and the Altiplano (Figures 7a and 7c; Figures S31 to S35), T-t paths for the
390 southern Eastern Cordillera (Ocobamba profile and individual data) suggest an increase in
391 cooling rate with values of $\sim 17^{\circ}\text{C}/\text{m.y.}$ between 7 and 3 Ma (Figure 7b; Figures S28 to S30 &
392 S36), in agreement with AERs (Figure 6).

393 For Pecube modeling, we display results from our thermo-kinematic inversions in 2D
394 graphics, where the explored parameter space is illustrated and each forward model is colored
395 by its respective misfit value (Figures 8, 9 and 10). For the entire Abancay Deflection model,
396 the basal temperature converges for values of 200°C to 700°C meaning geothermal gradient
397 of $6^{\circ}\text{C}/\text{km}$ to $23^{\circ}\text{C}/\text{km}$ (Text S1). The thermal diffusivity however, does not converge
398 (Figure 8). We present thereafter the best-fitting value for explored parameters within each
399 modeled crustal block. For the Altiplano model, parameter exploration through data inversion
400 reveals a clear inversion convergence for the output crustal-block exhumation rate at 0.2 ± 0.1
401 $\text{km}/\text{m.y.}$ (Figure 9a) with high reproducibility for thermochronological ages and time-
402 temperature paths (Figure 9b; Figure S41). The basal temperature does not converge but
403 presents four peaks at $420\pm 15^{\circ}\text{C}$, $480\pm 20^{\circ}\text{C}$, $525\pm 10^{\circ}\text{C}$ and $675\pm 30^{\circ}\text{C}$ (Figure 9a)
404 corresponding respectively to geothermal gradients of 14 ± 1 , 16 ± 1 , 17 ± 1 and $22\pm 1^{\circ}\text{C}/\text{km}$
405 (Text S1). Relief amplification factors do not converge neither and are non-determinative or
406 not discriminating (Figure S39). For the Eastern Cordillera model, the well-constrained value
407 for crustal-block exhumation is converging to 0.2 ± 0.1 $\text{km}/\text{m.y.}$ (Figure 10a), similarly to the
408 Altiplano's results. The lateral (north-south) position of the Apurimac fault system at 25 km
409 depth (x fault parameter) is constrained for an ideal value of -34 ± 5 km (the negative sign
410 corresponds to the northward exploration of this parameter). According to the approximate

411 surface trace of the Apurimac fault system and to the output of the x fault value, we estimated
412 a fault dip ranging between 28° to 47° toward the north (Figures 10a and 10d). Regarding the
413 fault kinetics, Pecube models favor fault activation at 5.3 ± 1.5 Ma with an associated fault
414 velocity of 2.9 ± 0.6 km/m.y. (Figure 10b). According to our estimate on fault dip and velocity
415 predictions, output exhumation rates of 1.2 ± 0.4 km/m.y. are predicted for the southern
416 Eastern Cordillera since ~ 5 Ma (Figure 10e). For the same time period, the northern Eastern
417 Cordillera and the Altiplano underwent steady exhumation rates (Figure 11). Finally, and
418 similarly to the Altiplano crustal-block model, relief amplification factor through time does
419 not converge for the Eastern Cordillera model (Figure S40). The thermochronological data
420 reproducibility is, however, excellent (Figure S42).

Table 2. Apatite (U-Th-Sm)/He data

Sample number	Morphology	Length (μm)	Width (μm)	Thickness (μm)	R_s (μm)	Weight (μg)	F_T	^4He (nccSTP/g)	^{238}U (ppm)	^{232}Th (ppm)	^{147}Sm (ppm)	Th/U	eU (ppm)	Age (Ma)	Corrected Age (Ma)	$\pm 1 \sigma$
<u>Ocobamba profile</u>																
AB-17-05A	2b	144	92	99	63	2.9	0.78	16932	29.3	21.5	80.5	0.7	35	4.1	5.2	0.4
AB-17-05B	2py	201	128	115	61	4.1	0.77	14156	40.5	25.2	84.6	0.6	47	2.5	3.3	0.3
AB-17-07A	1b + 1py	180	139	122	73	5.1	0.81	23568	65.6	41.9	98.1	0.6	76	2.6	3.2	0.3
AB-17-07B	2b	118	125	79	54	2.1	0.74	22253	45.1	26.1	93.4	0.6	52	3.6	4.9	0.4
AB-17-07C	2b	109	108	92	64	2.3	0.78	19309	58.3	35.4	107.4	0.6	67	2.4	3.1	0.2
AB-17-07D	2b	194	128	115	79	6.2	0.82	7087	36.2	26.3	92.8	0.7	43	1.4	1.7	0.1
AB-17-07E	1b + 1py	146	123	118	68	3.6	0.79	6820	32.2	20.5	82.4	0.6	38	1.5	1.9	0.2
AB-17-08A	2b	198	112	114	76	5.8	0.81	12131	63.8	29.1	88.9	0.5	71	1.4	1.7	0.1
AB-17-08B	1b + 1py	212	142	133	81	7.2	0.82	13951	70.6	18.7	89.3	0.3	76	1.5	1.9	0.1
AB-17-08C	1b + 1py	168	117	122	69	4.2	0.80	14539	56.3	27.4	85.2	0.5	63	1.9	2.4	0.2
AB-17-08D	1b + 1py	162	129	114	68	4.0	0.79	18175	59.2	19.0	81.6	0.3	64	2.4	3.0	0.2
AB-17-08E	1b + 1py	182	164	157	89	7.7	0.84	8668	47.2	17.1	72.9	0.4	52	1.4	1.7	0.1
AB-17-11A	1b + 1py	133	101	105	59	2.4	0.76	21106	111.0	213.5	89.7	1.9	163	1.1	1.4	0.1

Sample	Morphology	Length	Width	Thickness	R _s	Weight	F _T	⁴ He	²³⁸ U	²³² Th	¹⁴⁷ Sm	Th/U	eU	Age	Corrected Age	± 1 σ
number		(μm)	(μm)	(μm)	(μm)	(μg)		(nccSTP/g)	(ppm)	(ppm)	(ppm)		(ppm)	(Ma)	(Ma)	
AB-17-11B	2b	171	99	93	64	3.5	0.78	13654	65.5	157.8	72.5	2.4	104	1.1	1.4	0.1
AB-17-11C	1b + 1py	207	104	99	62	4.1	0.77	15283	107.9	190.1	76.6	1.8	154	0.8	1.1	0.1
AB-17-11E	2b	191	119	99	69	4.7	0.79	3626	29.4	55.0	27.3	1.9	43	0.7	0.9	0.1
<u>Individual data</u>																
AB-17-18A	2b	144	127	119	82	4.8	0.82	24984	10.8	39.4	40.9	3.6	21	10.2	12.4	1.0
AB-17-18B	2b	146	93	96	63	2.9	0.78	42585	19.6	68.4	52.4	3.5	36	9.8	12.7	1.0
AB-17-18C	2b	230	120	114	78	7.0	0.82	33557	12.0	41.1	37.7	3.4	22	12.8	15.6	1.3
AB-17-18E	2b	128	128	99	69	3.2	0.79	20493	8.3	27.5	35.9	3.3	15	11.4	14.4	1.2
AB-17-19A	2b	172	159	143	99	8.6	0.85	148729	122.7	5.9	55.9	0.1	124	9.9	11.6	0.9
AB-17-19B	2b	158	129	93	65	3.7	0.78	108144	103.9	11.9	48.2	0.1	107	8.4	10.7	0.9
AB-17-19I	2b	164	135	106	74	4.7	0.81	81674	58.3	4.8	32.2	0.1	60	11.3	14.0	0.8
<u>Lucma profile</u>																
AB-17-21A	1b + 1py	169	126	112	68	4.1	0.79	5878	50.8	144.1	61.4	2.8	86	0.6	0.7	0.1
AB-17-21C	2py	324	145	137	78	10.5	0.82	22398	55.6	290.9	91.1	5.2	126	1.5	1.8	0.1
AB-17-21D	2b	207	141	118	82	7.2	0.82	10613	35.4	102.9	40.6	2.9	60	1.5	1.8	0.1

Sample	Morphology	Length	Width	Thickness	R _s	Weight	F _T	⁴ He	²³⁸ U	²³² Th	¹⁴⁷ Sm	Th/U	eU	Age	Corrected Age	± 1 σ
number		(μm)	(μm)	(μm)	(μm)	(μg)		(nccSTP/g)	(ppm)	(ppm)	(ppm)		(ppm)	(Ma)	(Ma)	
AB-17-21E	1b + 1py	205	107	116	66	4.7	0.79	1580	4.7	15.7	5.3	3.3	9	1.6	2.0	0.2
AB-17-22B	1b + 1py	205	100	98	61	3.9	0.77	109443	72.5	16.5	83.3	0.2	77	11.8	15.4	1.2
AB-17-22C	2b	120	110	94	65	2.6	0.78	69585	47.1	87.0	103.1	1.8	68	8.5	10.9	0.9
AB-17-22D	2b	130	119	108	74	3.6	0.81	89394	60.5	14.5	71.9	0.2	64	11.5	14.3	1.1
AB-17-22E	1b + 1py	115	111	77	46	1.4	0.70	89806	71.4	14.5	56.4	0.2	75	9.9	14.2	1.1
AB-17-25A	2b	102	137	84	56	2.0	0.75	129728	39.0	3.5	80.0	0.1	40	26.9	35.8	2.9
AB-17-25C	2b	109	92	97	63	2.2	0.78	586257	183.9	18.4	104.7	0.1	189	25.7	33.2	2.7
AB-17-25D	2b	145	125	80	54	2.6	0.74	266746	82.9	19.7	93.8	0.2	88	25.2	34.0	2.7
AB-17-25E	1b + 1py	170	139	127	75	5.1	0.81	131857	47.2	7.5	43.2	0.2	49	22.2	27.4	2.2
AB-17-26A	2b	217	111	105	72	5.6	0.80	37130	17.4	5.0	67.6	0.3	19	16.4	20.5	1.6
AB-17-26C	2b	165	142	129	89	6.6	0.84	11233	9.0	3.3	42.7	0.4	10	9.5	11.3	0.9
AB-17-28A	2py	218	94	84	49	2.8	0.72	15300	40.8	142.5	69.7	3.5	75	1.7	2.4	0.2
AB-17-28B	2py	192	105	79	46	2.3	0.70	13444	23.5	90.8	55.5	3.9	46	2.5	3.5	0.3
AB-17-28C	1b + 1py	228	117	89	57	4.1	0.75	11401	34.8	125.5	57.5	3.6	65	1.5	1.9	0.2
AB-17-28D	2b	157	150	122	85	5.9	0.83	21690	93.9	77.5	56.6	0.8	113	1.6	1.9	0.2

Sample	Morphology	Length	Width	Thickness	R _s	Weight	F _T	⁴ He	²³⁸ U	²³² Th	¹⁴⁷ Sm	Th/U	eU	Age	Corrected Age	± 1 σ
number		(μm)	(μm)	(μm)	(μm)	(μg)		(nccSTP/g)	(ppm)	(ppm)	(ppm)		(ppm)	(Ma)	(Ma)	
AB-17-28E	1b + 1py	146	101	94	57	2.4	0.75	31059	31.3	121.4	59.5	3.9	61	4.3	5.7	0.5
<u>Limatambo profile</u>																
AB-17-29A	2b	173	109	100	69	4.1	0.79	46518	37.9	83.0	7.5	2.2	58	6.7	8.4	0.7
AB-17-29B	2b	151	132	114	79	4.8	0.82	44428	21.3	59.1	6.9	2.8	36	10.4	12.7	1.0
AB-17-29C	1b + 1py	165	92	89	54	2.5	0.74	37896	19.2	54.1	11.9	2.8	32	9.8	13.2	1.1
AB-17-29D	1b + 1py	140	116	103	61	2.8	0.77	42107	23.3	66.6	10.8	2.9	39	8.9	11.6	0.9
AB-17-29E	1b + 1py	149	110	112	64	3.2	0.78	19662	13.4	31.7	8.7	2.4	21	7.8	10.0	0.8
AB-17-30B	1b + 1py	148	92	84	52	2.1	0.73	31674	22.5	40.6	8.2	1.8	32	8.2	11.2	0.9
AB-17-30C	1b + 1py	170	133	104	64	3.8	0.78	29403	14.2	35.4	8.8	2.5	23	10.8	13.9	1.1
AB-17-31A	2b	189	104	114	72	4.9	0.80	12508	11.6	33.1	8.0	2.9	20	5.3	6.7	0.5
AB-17-31C	1b + 1py	153	112	99	60	2.9	0.77	10929	11.0	23.3	4.8	2.1	17	5.5	7.1	0.4
AB-17-31E	1b + 1py	185	103	100	61	3.6	0.77	14176	9.6	32.4	10.7	3.4	17	6.8	8.8	0.5
AB-17-32A	2b	140	114	103	71	3.6	0.80	12686	9.6	32.4	4.5	3.4	17	6.1	7.6	0.6
AB-17-32B	2b	140	111	106	73	3.7	0.80	17613	11.9	30.3	6.1	2.6	19	7.6	9.5	0.8
AB-17-33A	2py	155	109	100	50	2.2	0.72	8244	7.4	19.0	7.0	2.6	12	5.7	7.9	0.5

Sample	Morphology	Length	Width	Thickness	R _s	Weight	F _T	⁴ He	²³⁸ U	²³² Th	¹⁴⁷ Sm	Th/U	eU	Age	Corrected Age	± 1 σ
number		(μm)	(μm)	(μm)	(μm)	(μg)		(nccSTP/g)	(ppm)	(ppm)	(ppm)		(ppm)	(Ma)	(Ma)	
AB-17-33B	1b + 1py	161	152	175	85	6.4	0.83	13196	15.3	33.0	14.8	2.2	23	4.7	5.6	0.3
AB-17-33C	2b	175	115	102	71	4.5	0.80	19221	36.9	31.1	5.6	0.8	44	3.6	4.5	0.3
AB-17-33D	1b + 1py	234	118	103	66	5.2	0.78	25030	18.9	27.2	7.6	1.4	25	8.2	10.4	0.6
AB-17-33E	2b	133	119	104	72	3.5	0.80	13308	11.2	21.8	11.5	1.9	16	6.7	8.3	0.5
AB-17-34A	2b	154	118	113	77	4.6	0.81	12084	11.3	29.9	9.2	2.6	19	5.4	6.7	0.5
AB-17-34B	2b	155	152	126	87	6.2	0.84	7372	7.6	27.1	7.7	3.6	14	4.4	5.2	0.4
AB-17-34C	2b	179	127	134	87	6.7	0.83	7112	10.3	31.9	17.8	3.1	18	3.3	4.0	0.3
AB-17-34D	1b + 1py	139	93	95	55	2.2	0.75	5905	8.1	19.5	5.5	2.4	13	3.8	5.1	0.4
AB-17-34E	2b	180	104	97	67	4.0	0.79	5074	6.8	26.9	11.2	3.9	13	3.2	4.0	0.3
AB-17-35D	1b + 1py	203	122	97	62	4.1	0.77	5720	15.3	25.9	8.9	1.7	22	2.2	2.9	0.2
AB-17-35E	2b	142	104	96	66	3.1	0.78	12729	11.6	30.8	6.1	2.7	19	5.6	7.1	0.6
AB-17-36A	1b + 1py	142	103	105	60	2.7	0.77	9698	23.5	41.8	8.5	1.8	34	2.4	3.1	0.3
AB-17-36D	1b + 1py	160	108	100	60	3.0	0.77	5544	9.4	32.3	6.6	3.4	17	2.7	3.5	0.3
AB-17-36E	1b + 1py	186	128	123	74	5.2	0.81	3274	12.6	37.8	10.5	3.0	22	1.3	1.6	0.1

Abancay profile

Sample	Morphology	Length	Width	Thickness	R _s	Weight	F _T	⁴ He	²³⁸ U	²³² Th	¹⁴⁷ Sm	Th/U	eU	Age	Corrected Age	± 1 σ
number		(μm)	(μm)	(μm)	(μm)	(μg)		(nccSTP/g)	(ppm)	(ppm)	(ppm)		(ppm)	(Ma)	(Ma)	
AB-17-37A	2py	242	123	125	67	5.8	0.79	70766	88.7	113.0	23.4	1.3	116	5.1	6.4	0.5
AB-17-37B	2b	117	113	102	70	2.9	0.80	72471	82.8	104.3	22.2	1.3	108	5.6	7.0	0.6
AB-17-37C	1b + 1py	252	139	111	71	6.8	0.80	51165	63.5	75.0	12.2	1.2	82	5.2	6.5	0.5
AB-17-37D	1b + 1py	189	132	100	57	3.5	0.75	38099	44.3	45.9	18.3	1.0	56	5.7	7.6	0.6
AB-17-38A	1b + 1py	240	121	128	75	6.9	0.81	53821	50.9	59.8	15.8	1.2	65	6.8	8.5	0.7
AB-17-38B	1b + 1py	254	132	144	82	8.8	0.83	52415	52.3	56.4	16.8	1.1	66	6.6	8.0	0.6
AB-17-38C	2py	297	144	152	80	10.2	0.82	67076	70.5	75.4	18.4	1.1	89	6.3	7.6	0.6
AB-17-38D	1b + 1py	260	133	149	83	9.3	0.83	77615	74.9	87.9	19.9	1.2	96	6.7	8.1	0.6
AB-17-38E	1b + 1py	202	119	97	61	4.0	0.77	13309	21.2	40.3	13.1	1.9	31	3.6	4.6	0.4
AB-17-39C	1b + 1py	190	129	132	77	5.8	0.81	55767	61.8	41.0	27.6	0.7	72	6.4	7.9	0.6
AB-17-39D	2py	185	109	99	53	2.9	0.74	95376	116.8	113.2	19.5	1.0	144	5.5	7.4	0.6
AB-17-40A	1b + 1py	237	118	124	73	6.6	0.81	137948	171.0	73.7	33.9	0.4	189	6.1	7.5	0.6
AB-17-40B	2py	209	115	113	60	4.1	0.77	50558	68.0	69.9	28.2	1.0	85	4.9	6.5	0.5
AB-17-40C	1b + 1py	247	128	137	79	8.0	0.82	92739	112.4	67.5	28.2	0.6	129	6.0	7.3	0.6
AB-17-40D	2py	228	156	161	76	7.5	0.81	103926	113.9	73.5	28.6	0.6	132	6.5	8.1	0.6

Sample	Morphology	Length	Width	Thickness	R _s	Weight	F _T	⁴ He	²³⁸ U	²³² Th	¹⁴⁷ Sm	Th/U	eU	Age	Corrected Age	± 1 σ
number		(μm)	(μm)	(μm)	(μm)	(μg)		(nccSTP/g)	(ppm)	(ppm)	(ppm)		(ppm)	(Ma)	(Ma)	
AB-17-40E	1b + 1py	197	128	104	65	4.5	0.78	49030	70.7	42.0	14.7	0.6	81	5.0	6.4	0.5
AB-17-41A	1b + 1py	224	131	125	77	6.8	0.81	25929	13.0	21.9	17.4	1.7	18	11.8	14.5	1.2
AB-17-41B	1b + 1py	115	103	95	55	1.8	0.74	50384	18.0	17.6	10.3	1.0	22	18.8	25.3	2.0
AB-17-41C	2py	220	121	104	58	4.1	0.76	40105	19.7	21.8	16.2	1.1	25	13.3	17.6	1.4
AB-17-41D	2b	160	111	134	77	4.9	0.81	27300	10.1	26.9	17.6	2.7	17	13.7	16.8	1.3
AB-17-41E	1b + 1py	187	137	122	74	5.4	0.81	37150	23.1	9.4	5.2	0.4	25	12.1	15.0	1.2
AB-17-42A	2b	180	128	122	83	6.3	0.83	67778	44.1	34.7	13.7	0.8	52	10.7	12.9	1.0
AB-17-42B	2b	145	132	125	86	5.3	0.83	25104	18.5	20.0	22.4	1.1	23	8.9	10.7	0.9
AB-17-42C	2py	216	109	113	59	4.1	0.76	100130	68.3	52.9	14.8	0.8	81	10.2	13.4	1.1
AB-17-42D	1b + 1py	177	101	123	63	3.7	0.77	72476	48.0	28.3	11.8	0.6	55	10.9	14.1	1.1
AB-17-43A	1b + 1py	166	108	90	56	2.8	0.75	49427	40.8	7.3	12.7	0.2	43	9.6	12.8	1.0
AB-17-43C	2b	162	93	85	58	2.8	0.76	35909	33.7	5.4	19.1	0.2	35	8.5	11.2	0.9
AB-17-43D	2b	197	92	100	63	3.9	0.77	49624	45.3	25.0	20.1	0.6	52	8.0	10.3	0.8
AB-17-43E	2b	164	97	93	63	3.3	0.78	43734	52.5	20.7	10.1	0.4	58	6.3	8.1	0.6
AB-17-44A	1b + 1py	214	112	101	63	4.5	0.78	144444	129.5	14.1	13.7	0.1	133	9.0	11.6	0.9

Sample number	Morphology	Length (μm)	Width (μm)	Thickness (μm)	R _s (μm)	Weight (μg)	F _T	⁴ He (nccSTP/g)	²³⁸ U (ppm)	²³² Th (ppm)	¹⁴⁷ Sm (ppm)	Th/U	eU (ppm)	Age (Ma)	Corrected Age (Ma)	± 1 σ
AB-17-44B	1b + 1py	100	114	181	60	2.1	0.76	86599	83.7	19.7	7.7	0.2	88	8.1	10.6	0.8
AB-17-44C	2b	184	139	114	79	6.0	0.82	76257	76.9	12.9	9.1	0.2	80	7.9	9.6	0.8
AB-17-44D	1b + 1py	154	110	102	61	3.0	0.77	94100	95.5	39.5	18.5	0.4	105	7.4	9.6	0.8
AB-17-44E	2b	136	110	110	74	3.7	0.81	134264	88.5	52.8	17.6	0.6	101	11.0	13.6	1.1
<u>Incahuasi profile</u>																
AB-17-55A	1b + 1py	213	157	139	84	8.0	0.83	5526	21.0	37.7	40.6	1.8	30	1.5	1.8	0.1
AB-17-55B	1b + 1py	198	117	110	68	4.7	0.79	6030	28.8	47.5	47.3	1.6	40	1.2	1.6	0.1
AB-17-55C	2py	221	117	102	58	4.0	0.76	10533	32.4	50.0	51.4	1.5	45	2.0	2.6	0.2
AB-17-55D	2b	183	129	125	85	6.6	0.83	5988	21.5	36.6	52.4	1.7	31	1.6	2.0	0.2
AB-17-55E	1b + 1py	196	138	132	79	6.4	0.82	4848	27.3	41.8	43.6	1.5	38	1.1	1.3	0.1

Note: Morphology refers to the apatite geometry. 2py: 2 hexagonal pyramids; 2b: 2 broken faces; 1b + 1py: 1 broken face & 1 hexagonal pyramid (Brown et al., 2013).

F_T is the alpha ejection correction factor and R_s is the sphere equivalent radius of hexagonal crystal (Gautheron et al., 2012; Ketcham et al., 2011).

422

423

424

Table 3. Apatite fission-track data

Sample number	n	ρ_s (10^5 cm^{-2})	N_s	ρ_i (10^5 cm^{-2})	N_i	ρ_d (10^5 cm^{-2})	$P(\chi^2)$	Dispersion (%)	Central age (Ma)	$\pm 2 \sigma$	U (ppm)	$\pm 1 \sigma$	n D_{par}	MDpar (μm)	n TL	MTL (μm)
<u>Ocobamba profile</u>																
AB-17-05	23	0.99	(140)	27.7	(3915)	12.0	100.0	0.0	5.9	1.1	35	2	88	1.09	6	11.43
AB-17-06	24	0.47	(69)	21.3	(3155)	12.0	99.3	0.1	3.6	0.9	27	1	82	1.12	3	12.34
AB-17-07	22	0.64	(90)	29.2	(4098)	12.0	84.6	0.4	3.6	0.8	36	1	68	1.27	5	10.92
AB-17-08	25	0.85	(136)	40.6	(6486)	12.0	93.6	0.2	3.5	0.7	51	2	106	1.16	12	11.48
AB-17-11	20	0.73	(79)	34.3	(3725)	12.1	99.7	0.1	3.5	0.8	43	2	96	1.30	1	9.8
<u>Individual data</u>																
AB-17-13	30	0.65	(106)	18.3	(3007)	12.1	100.0	0.0	5.9	1.3	23	1	66	1.24	5	10.76
AB-17-15	26	0.07	(9)	4.15	(568)	12.1	99.3	0.2	2.6	1.9	5	0	52	1.18	N.D.*	N.D.*
AB-17-18	25	1.01	(160)	6.82	(1081)	12.1	100.0	0.1	24.7	4.6	8	1	109	1.53	3	10.83
AB-17-19	25	4.32	(476)	34.2	(3762)	12.2	87.0	0.3	21.1	2.7	42	2	139	1.29	10	11.48
<u>Lucma profile</u>																
AB-17-22	22	3.98	(388)	33.7	(3285)	12.2	87.1	0.3	19.8	2.7	41	2	115	1.15	5	10.87
AB-17-23	18	6.79	(314)	46.4	(2090)	12.2	47.4	6.9	25.2	3.8	57	3	92	1.16	7	11.72

Sample number	n	ρ_s (10^5 cm^{-2})	N_s (901)	ρ_i (10^5 cm^{-2})	N_i (3979)	ρ_d (10^5 cm^{-2})	$P(\chi^2)$ 51.7	Dispersion (%)	Central age (Ma)	$\pm 2 \sigma$	U (ppm)	$\pm 1 \sigma$	n D_{par}	MDpar (μm)	n TL	MTL (μm)
AB-17-25	18	16.5	(901)	73.0	(3979)	12.3	51.7	4.0	38.2	4.4	89	3	121	1.80	7	13.59
AB-17-26	24	2.95	(286)	24.8	(2393)	12.3	99.9	0.1	20.2	3.0	30	1	117	1.21	7	11.64
<u>Limatambo profile</u>																
AB-17-29	19	4.97	(307)	24.8	(1532)	13.8	96.0	0.1	37.9	5.7	27	2	96	1.65	8	11.99
AB-17-31	20	1.52	(109)	10.6	(764)	13.8	94.6	0.3	27.1	5.9	12	1	116	1.32	3	12.15
AB-17-32	20	1.90	(133)	14.5	(1017)	13.9	98.5	0.1	24.9	5.0	16	1	151	1.42	2	11.69
AB-17-33	22	1.87	(159)	17.6	(1499)	13.9	93.1	0.2	20.2	3.8	19	1	117	1.19	3	12.46
AB-17-36	18	1.95	(120)	16.3	(1000)	14.0	66.4	0.6	23.0	4.8	17	1	70	1.30	3	10.68
<u>Abancay profile</u>																
AB-17-37	20	4.44	(244)	50.6	(2778)	14.0	100.0	0.1	16.9	2.6	54	2	103	1.24	3	12.10
AB-17-38	20	6.94	(647)	69.4	(6470)	14.0	100.0	0.0	19.3	2.3	74	2	113	2.15	18	12.43
AB-17-39	20	4.77	(506)	49.6	(5262)	14.1	99.9	0.1	18.6	2.4	53	2	102	1.57	5	11.38
AB-17-40	20	5.73	(532)	62.9	(5837)	14.1	92.2	0.1	17.6	2.2	67	2	80	1.47	7	10.94
AB-17-41	26	3.27	(544)	18.3	(3041)	14.1	99.9	0.1	34.6	4.3	19	1	118	1.42	N.D.*	N.D.*
AB-17-42	26	5.48	(764)	34.1	(4761)	14.1	87.2	0.6	31.1	3.6	36	1	137	1.46	7	11.72

Sample number	n	ρ_s (10^5 cm^{-2})	N_s	ρ_i (10^5 cm^{-2})	N_i	ρ_d (10^5 cm^{-2})	$P(\chi^2)$	Dispersion (%)	Central age (Ma)	$\pm 2 \sigma$	U (ppm)	$\pm 1 \sigma$	n D_{par}	MDpar (μm)	n TL	MTL (μm)
AB-17-44	25	5.15	(632)	44.6	(5477)	14.2	98.1	0.2	22.4	2.7	47	2	146	1.70	21	11.37
<u>Incahuasi profile</u>																
AB-17-51	14	0.45	(18)	9.66	(389)	14.2	12.7	44.0	9.0	5.2	10	1	32	1.41	N.D.*	N.D.*
AB-17-55	27	0.88	(64)	25.1	(1833)	14.2	9.0	39.1	6.6	2.1	26	1	108	0.98	6	10.71
<u>Previous studies</u>																
LK95/200 [†]	30	N.R. [§]	N.R. [§]	N.R. [§]	N.R. [§]	N.R. [§]	46.5	N.R. [§]	2.2	0.5	N.R. [§]	N.R. [§]	N.R. [§]	N.R. [§]	N.R. [§]	N.R. [§]
LK95/202 [†]	30	N.R. [§]	N.R. [§]	N.R. [§]	N.R. [§]	N.R. [§]	97.0	N.R. [§]	2.4	0.5	N.R. [§]	N.R. [§]	N.R. [§]	N.R. [§]	N.R. [§]	N.R. [§]
Pi6.1 [#]	23	2.27	(456)	20.7	(4159)	11.0	10.0	N.R. [§]	22.5	N.R. [§]	23	2	40	2.68	41	11.21
Pi6.2 [#]	16	1.55	(168)	13.8	(1491)	10.9	100.0	N.R. [§]	22.0	N.R. [§]	17	2	20	2.78	31	13.40
Pi6.3 [#]	20	1.74	(323)	16.2	(3005)	10.8	99.5	N.R. [§]	20.8	N.R. [§]	18	1	44	2.87	37	14.04
Pi6.4 [#]	20	0.69	(137)	6.21	(1242)	10.7	98.0	N.R. [§]	21.1	N.R. [§]	7	2	28	2.37	46	12.76
Pi6.5 [#]	19	0.79	(148)	9.05	(1701)	10.6	100.0	N.R. [§]	16.5	N.R. [§]	10	2	43	2.55	34	13.13
Pi6.6 [#]	20	1.04	(203)	12.0	(2354)	10.5	87.0	N.R. [§]	16.2	N.R. [§]	14	1	31	2.61	21	13.36
Pi6.7 [#]	20	1.09	(141)	12.7	(1637)	10.4	93.0	N.R. [§]	16.0	N.R. [§]	16	2	23	2.72	35	12.89
Pi6.8 [#]	20	0.86	(140)	10.2	(1662)	10.3	93.0	N.R. [§]	15.5	N.R. [§]	12	2	17	2.98	30	12.45

Sample number	n	ρ_s (10^5 cm^{-2})	N_s	ρ_i (10^5 cm^{-2})	N_i	ρ_d (10^5 cm^{-2})	$P(\chi^2)$	Dispersion (%)	Central age (Ma)	$\pm 2 \sigma$	U (ppm)	$\pm 1 \sigma$	n D_{par}	MDpar (μm)	n TL	MTL (μm)
---------------	---	--	-------	--	-------	--	-------------	-------------------	---------------------	----------------	---------	----------------	-----------------------	----------------------------	---------	--------------------------

Note: Fission-track age is given as Central Age (Galbraith & Laslett, 1993). Samples were counted dry with a BX51 Olympus microscope at 1250x magnification. Ages were calculated with the BINOMFIT program (T. A. Ehlers et al., 2005), using a zeta value of 275.18 ± 11.53 and the IRMM 540 uranium glass standard (15 ppm U). MDpar = mean Dpar value, MTL = mean track lengths of horizontally confined tracks.

*N.D. = no data

†Previous data (Kennan, 2008). For samples LK95/200 and LK95/202, elevations are respectively 3.1 and 2.1 km.

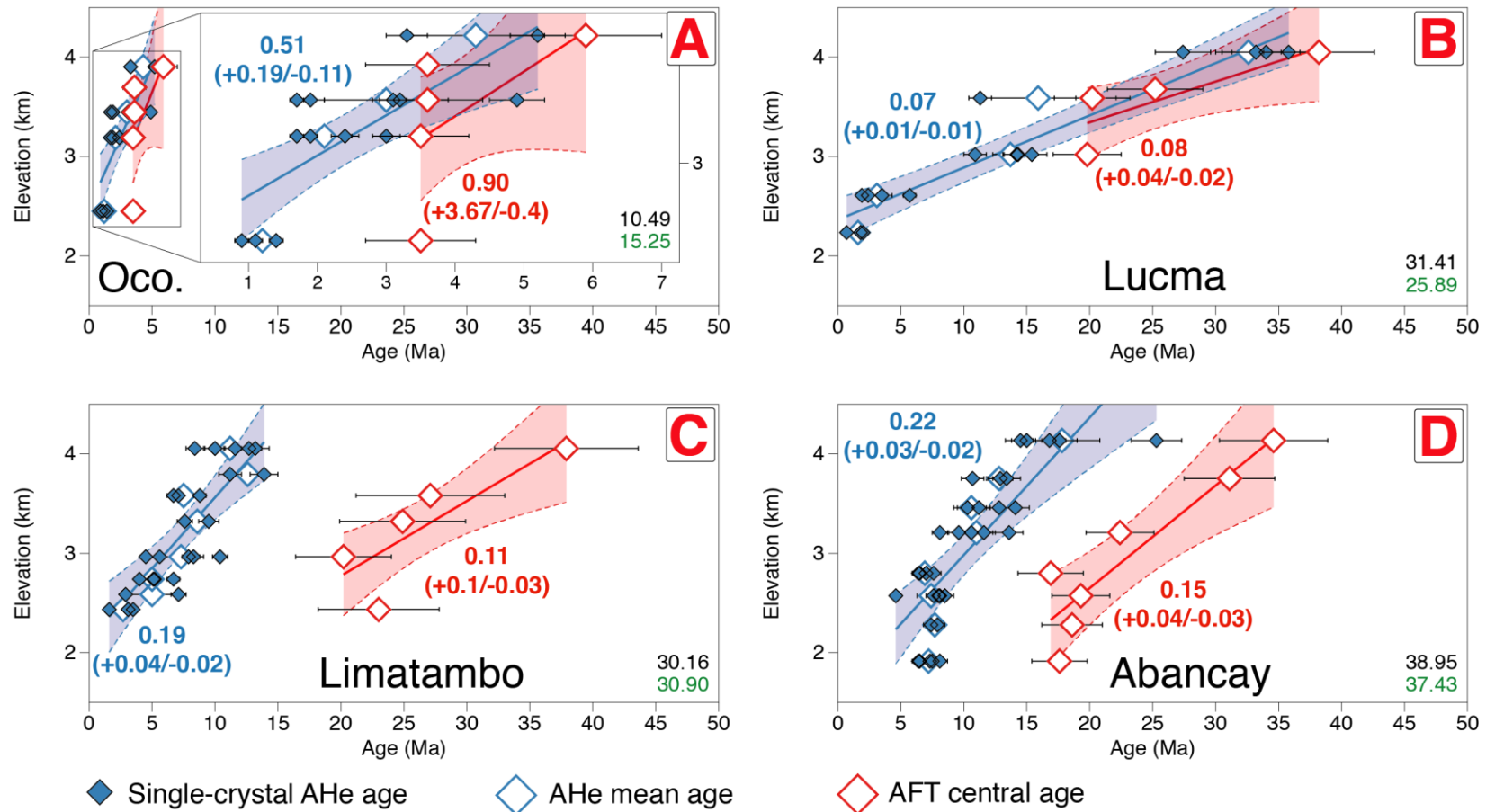
§N.R. = not reported

Previous data from Ruiz et al. (2009) for samples Pi6.1 (3.87 km); Pi6.2 (3.80 km); Pi6.3 (3.65 km); Pi6.4 (3.45 km); Pi6.5 (3.25 km); Pi6.6 (3.10 km); Pi6.7 (3.00 km); and Pi6.8 (2.85 km).

426

427

428



429

430

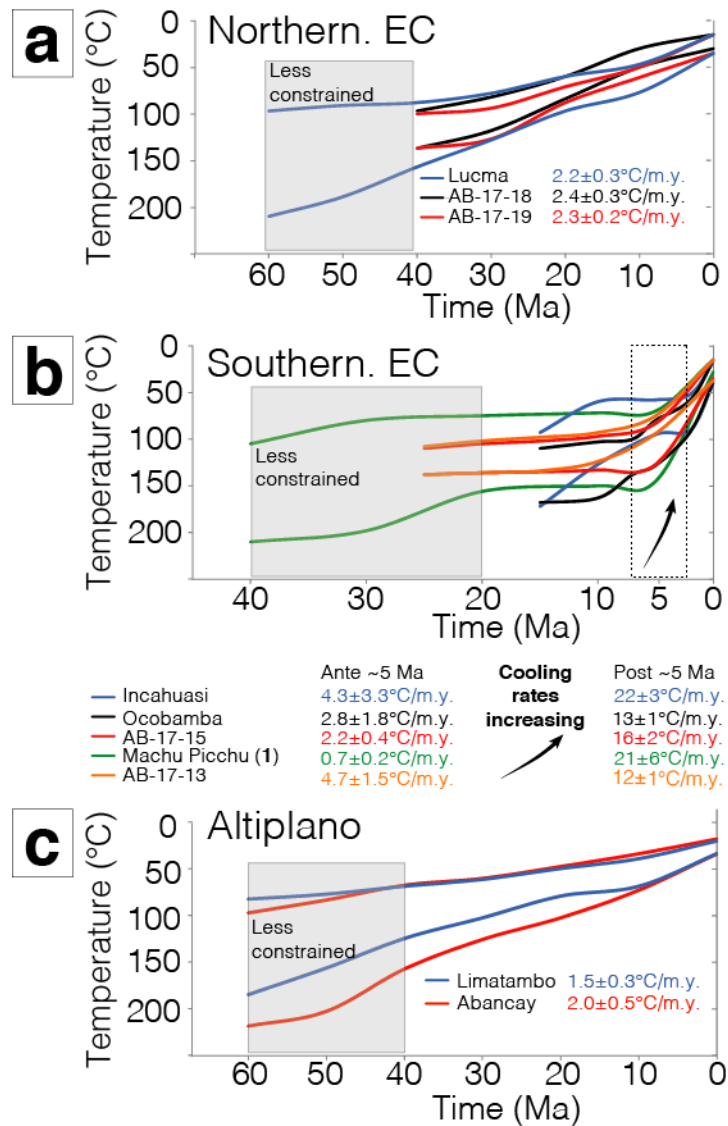
431

432

433

434

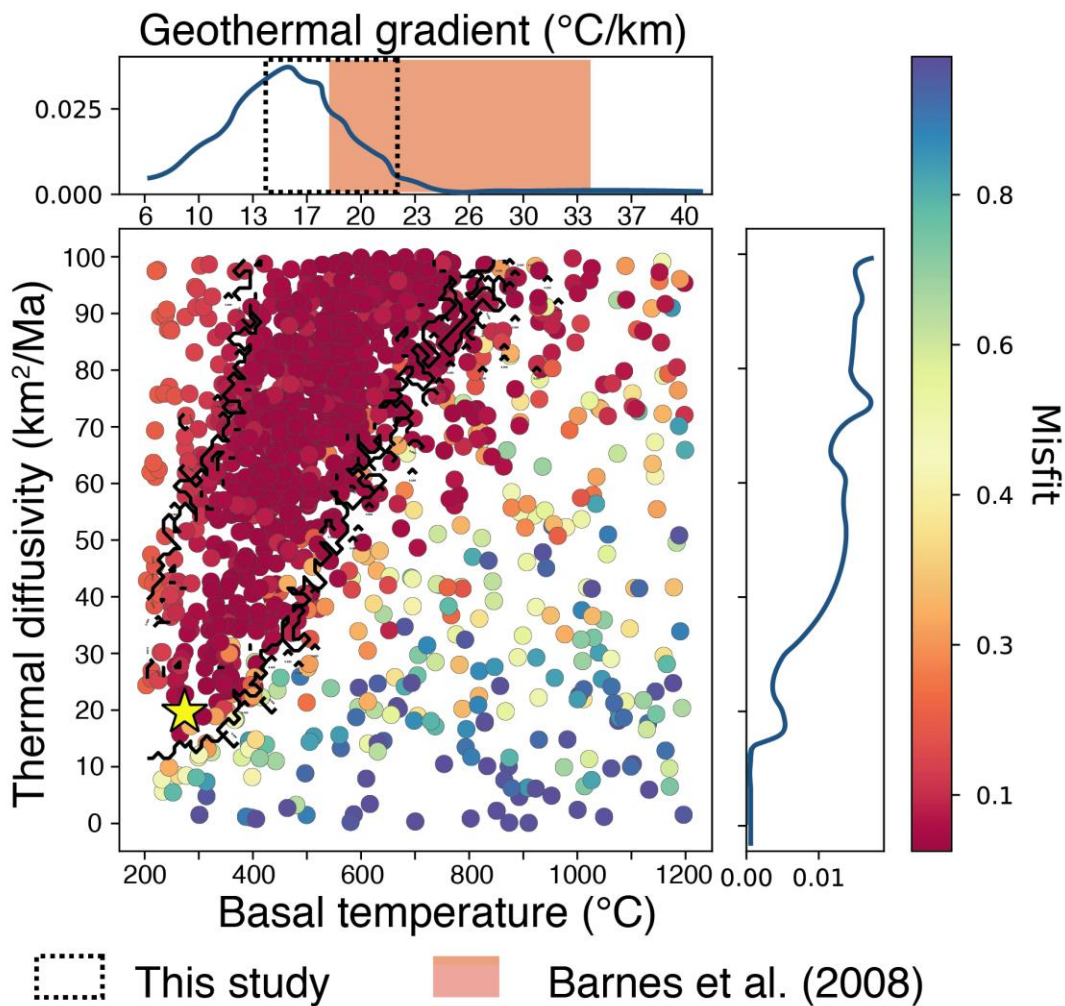
Figure 6. Age-Elevation plots (AHe & AFT ages) for the vertical profiles of Ocobamba (A; Oco.), Lucma (B), Limatambo (C) and Abancay (D) (see Figure 4 for profiles location). Blue diamonds are single-grain AHe ages, open diamonds are mean AHe (blue) and central AFT (red) ages. Blue and red numbers on the graphics refer to AER apparent exhumation rates (km/m.y.) respectively for AHe and AFT ages. Blue and red dashed lines correspond to minimum and maximum values for exhumation rates (AER; 95% confidence interval). BIC values for AHe and AFT data are respectively indicated in black and green on plots.



435

436 **Figure 7.** Time-temperature paths derived from QTQt inverse modeling of
 437 thermochronological data (Gallagher, 2012). a, b and c: Synthesis of time-temperature paths
 438 (colored lines) derived from QTQt (95 % reliability). Colored numbers in legend refer to the
 439 output cooling rates. See the [Supporting information](#) for details regarding the data
 440 reproducibility (observed vs. predicted data). a, b and c respectively correspond to samples in
 441 the northern Eastern Cordillera (EC), the southern Eastern Cordillera and the Altiplano (see
 442 [Figure 4](#) for location). In b, number 1 (Machu Picchu profile) refers to [Gérard et al.](#)
 443 [submitted](#).

444



445

446

447

448

449

450

451

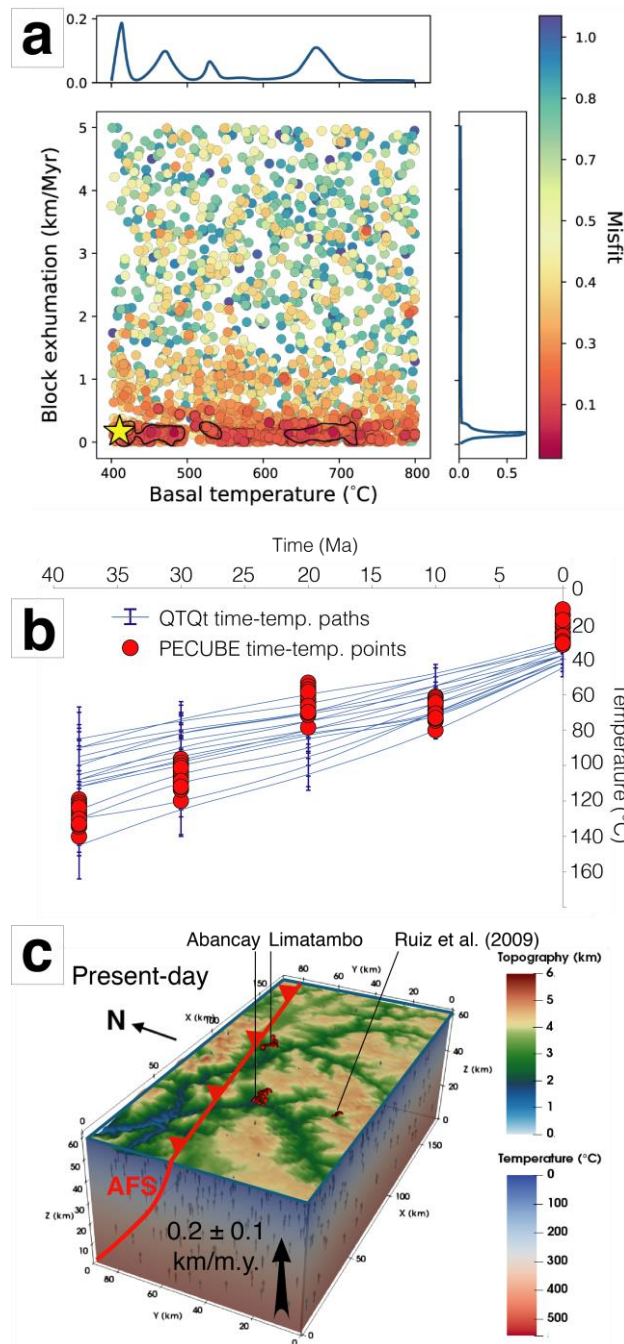
452

453

454

455

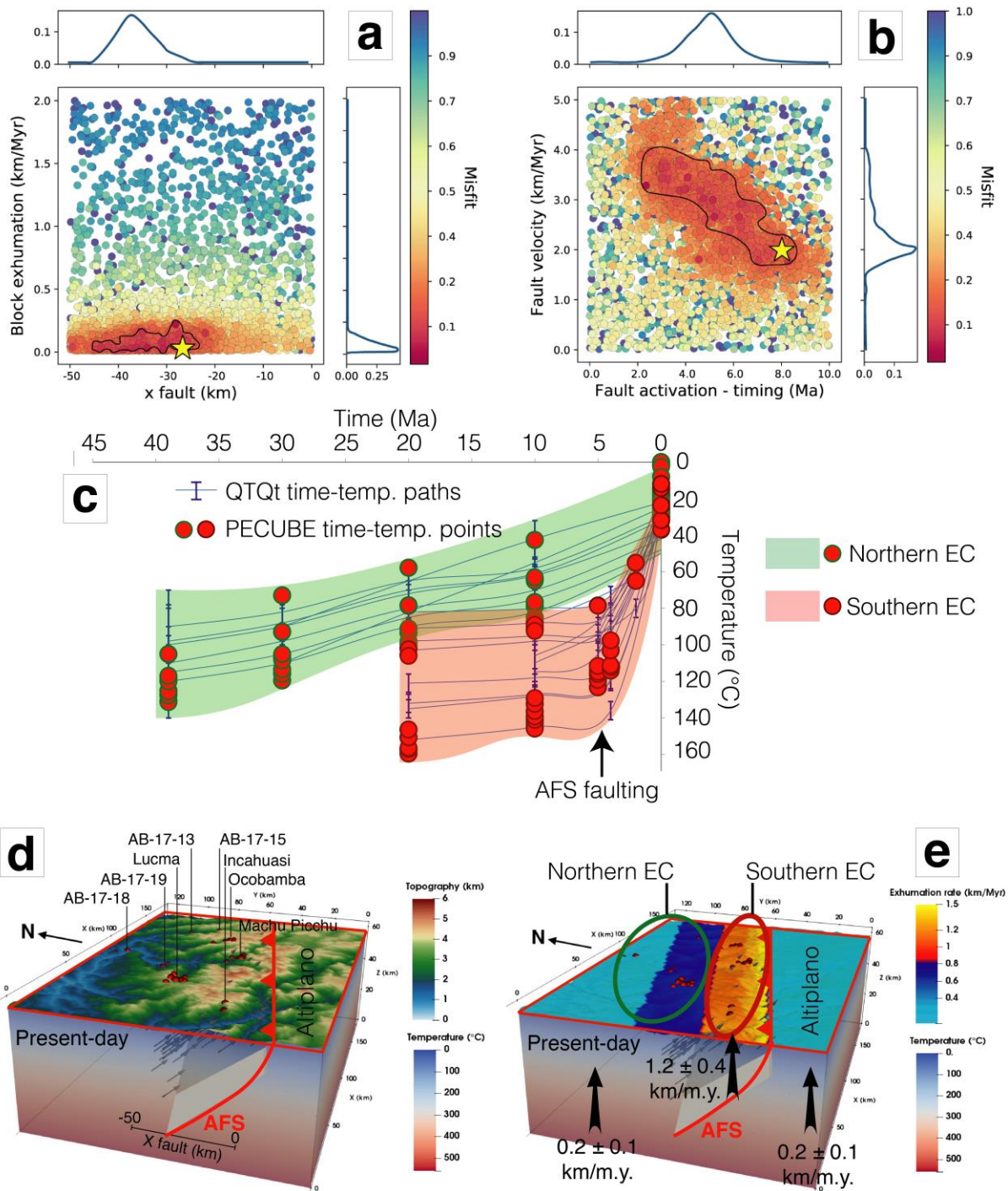
Figure 8. 3D Pecube inversion results regarding the thermal structure of the crust for the merged Altiplano and Eastern Cordillera crustal blocks. The graphic shows 2D parameter space and inversion results for thermal diffusivity vs. basal temperature. Each colored point corresponds to one forward model. The total sample size for inverse modeling is 1200. Blue curves (up and right subpanels) are the probability density for each parameter. The yellow star is the best-fitting model. The thermal diffusivity does not converge. We thus converted the basal temperature into geothermal gradients ([Text S1](#)) using a fixed thermal diffusivity of 40 ± 11 km²/Ma (compiled from Arndt et al., 1997 and Whittington et al., 2009). We compared these geotherms to our estimated range, and the one compiled by Barnes et al. (2008) (top panel).



456

457 **Figure 9.** 3D Pecube inversion results for the Altiplano crustal block. a) 2D parameter space
 458 and inversion results for crustal-block exhumation vs. basal temperature. Each colored point
 459 corresponds to one forward model. Blue curves (up and right subpanels) are the probability
 460 density for each parameter. The yellow star is the best-fitting model. b) Direct comparison of
 461 time-temperature paths derived from QTQt and ones computed with Pecube best-fitting
 462 model. c) Crustal-block model for the Altiplano (see [Figure 2](#) for location) with locations of
 463 thermochronological data.

464



465

466 **Figure 10.** 3D Pecube inversion results for the Eastern Cordillera crustal block. a) 2D
 467 parameter space and inversion results for crustal-block exhumation vs. position of the fault at
 468 25 km-depth (x fault parameter). b) 2D parameter space and inversion results for the fault
 469 velocity vs. activation timing of the Apurimac fault system. Each colored point corresponds
 470 to one forward model. Blue curves (up and right subpanels) are the probability density for

471 each parameter. The yellow stars in panels a and b are the best-fitting model. c) Direct
472 comparison of time-temperature paths derived from QTQt and ones computed with Pecube
473 best-fitting model. d) Crustal-block model for the Eastern Cordillera with locations of
474 thermochronological data (see [Figure 2](#) for location). e) Surface exhumation pattern for the
475 Eastern Cordillera since ~5 Ma predicted from Pecube best-fitting model. AFS is the
476 Apurimac fault system.

477

478 **5 Discussion**

479 **5.1 From cooling rate to exhumation rate**

480 Modeled thermal histories obtained from the Abancay Deflection area present only a
481 monotonic cooling phase with variable cooling rates ([Figure 7](#)). Those thermal histories do
482 not record any reheating event ([Figure 7](#)), which simplifies our modeling approach regarding
483 the crustal thermal structure. This confirms that the thermal perturbation supposedly
484 associated with the magmatic arc activity between 50 and 30 Ma (Mamani et al., 2010) is not
485 registered in our local thermochronological record. This can be explained by three reasons: 1)
486 present-day outcropping rocks were at that time still at depth and thus above the PRZ/PAZ,
487 not impacted by this reheating event; 2) for the southern Eastern Cordillera, the high
488 exhumation rates may have erased any older thermal signal; and 3) the thermal perturbation
489 was potentially spatially and/or temporally localized and did not affect our sampled sites.

490 Because we did not detect any perturbation of thermal histories by reheating or
491 potential isotherm relaxations (the sampled rocks were deep enough at that time), we convert
492 the inferred cooling scenario into simple exhumation histories. Exhumation rates estimated
493 using the obtained cooling rates derived from QTQt thermal modeling using a steady and
494 spatially-uniform geothermal gradient ($18\pm 4^\circ\text{C}/\text{km}$), apparent exhumation rates from AERs
495 (Glotzbach et al., 2011) and Pecube inversions results present consistent exhumation values

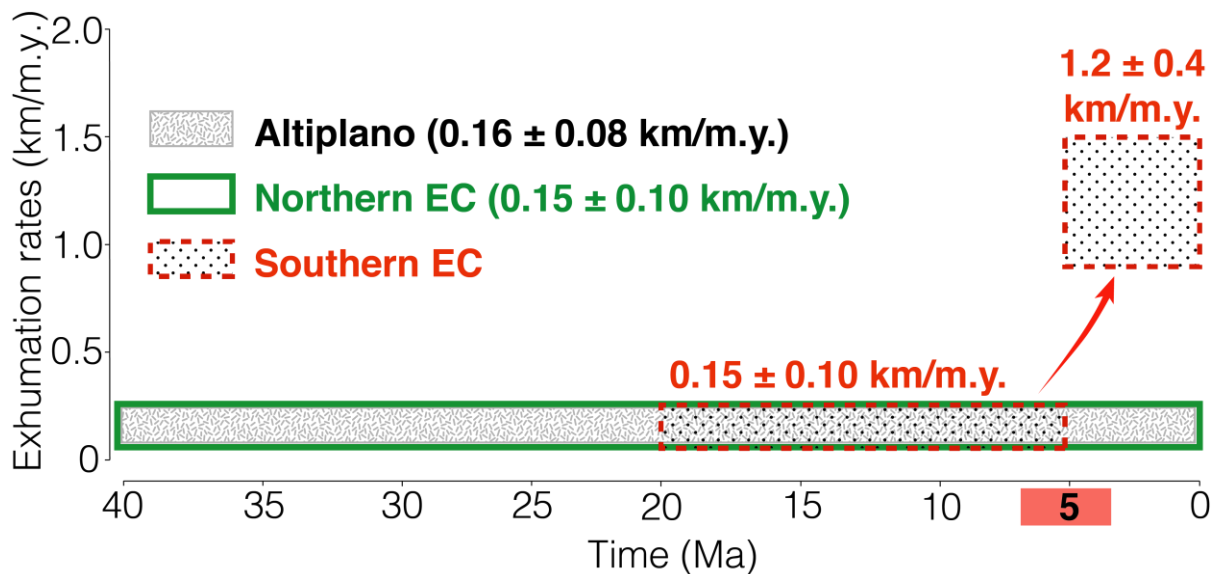
496 and high data reproducibility between three independent approaches (Figure S43). This
497 confirms that the assumed geothermal gradients for QTQt and Pecube models are
498 satisfactory, even if we cannot tightly constrain the basal crustal temperature from Pecube
499 inversion (Figures 8 and 9a). This non-convergence issue is frequently encountered in this
500 type of modeling (e.g. Robert et al., 2011; Valla et al., 2012) and can be bypassed only by
501 imposing thermal parameter values that fit the regional geothermal gradient. In details, we
502 notwithstanding identified four temperature peaks (probability density function for the
503 Altiplano model; Figure 9a), corresponding to geothermal gradients spanning from 13°C/km
504 to 23°C/km, compatible with the one we computed of $18\pm 4^\circ\text{C}/\text{km}$, and the one obtained
505 inverting thermal parameters for the entire Abancay Deflection (Figure 8). We furthermore
506 performed inversion of given parameters for each crustal model (Altiplano and Eastern
507 Cordillera blocks; Table S4; Text S5), imposing a “warmer” geothermal gradient ($30^\circ\text{C}/\text{km}$;
508 Text S5). It clearly appears that the $\sim 20^\circ\text{C}/\text{km}$ geothermal gradient seems to be the most
509 likely option for the Abancay Deflection at the scale of our study with better
510 thermochronological data reproducibility (Text S5; Figures S45 and S46).

511 We separated the study area in three zones derived from the exhumation rate output
512 patterns (QTQt; Figure 4 and 7). Using results obtained from Pecube, the Altiplano and the
513 northern Eastern Cordillera experienced similar exhumation histories since 40 Ma with
514 exhumation rates of $\sim 0.15\pm 0.10$ km/m.y. (Figure 11). The southern Eastern Cordillera
515 experienced the same exhumation rate from ~ 20 to 5.3 ± 1.5 Ma, followed by an acceleration
516 of exhumation to 1.2 ± 0.4 km/m.y. (Figure 11). Even though the thermochronological-data
517 modeling and output time-temperature paths from QTQt are limited to the last 20 Ma for the
518 southern Abancay Deflection (Figures 7b and 10c), we propose by temporal extrapolation
519 that the southern Eastern Cordillera underwent similar exhumation rates as its neighboring
520 areas (i.e. Altiplano and northern Eastern Cordillera) between 40 and 20 Ma. Over the last ~ 5

521 Ma, the exhumation acceleration is spatially framed southward by the Apurimac fault system,
 522 pointing towards a differential exhumation pattern in the Abancay Deflection that we
 523 attribute to tectonically driven surface uplift along the Apurimac fault system, and removal of
 524 rocks by erosion.

525

526



527

528 **Figure 11.** Exhumation rates derived from Pecube for the Abancay Deflection through time.

529 Each color corresponds to the three exhumation areas identified in this study. Details
 530 regarding the computed values for exhumation rates according to AERs, QTQt and Pecube
 531 are available in the [Figure S43](#).

532

533 5.2 Exhumation of the Abancay Deflection between 40 and 5 Ma

534 The whole Abancay Deflection region experienced steady, moderate (0.2 ± 0.1
 535 km/m.y) and apparently spatially uniform exhumation between 40 and 5 Ma ([Figures 11](#) and
 536 [12](#)). This exhumation rate is highly consistent with those inferred between 40 and 15 Ma
 537 from the only thermochronological data available in the area (0.17 km/m.y.; Ruiz et al.,
 538 2009). Even if the Peruvian Altiplano experienced Miocene faulting delimitating intra-

539 mountainous basins (Tinajani, Punacancha, and Paruro basins; Carlotto, 2013; Horton et al.,
540 2014), there is no evidence for any acceleration of exhumation related to these crustal
541 processes. Surprisingly, although the Bolivian Eastern Cordillera registered peaks of
542 exhumation through tectonic and erosional processes between 50 and 15 Ma (Barnes et al.,
543 2012), our data and inverse models favor a large-scale uniform exhumation history during
544 that period.

545 Consequently, we interpret the steady and uniform exhumation rates as the record of
546 low-magnitude surface denudation affecting the Abancay Deflection in an internally-drained
547 environment (Figure 12). Furthermore, contemporaneously to the Bolivian Orocline bending
548 during Miocene (Roperch et al., 2006), the Abancay Deflection was built in a left-lateral
549 transpressional context (Dalmayrac et al., 1980) associated to lateral rock advection from the
550 south (Figure 12c and 12d). The crustal tectonic regime, dominated by horizontal motion,
551 cannot be registered by the thermochronological data, nor easily-modeled by balanced cross-
552 section that encompass only 2D processes (Gotberg et al., 2010). Moreover, our outcomes
553 pointing towards a low-magnitude exhumation rate of ~ 0.2 km/m.y. between 40 and 5 Ma are
554 comparable in term of magnitude with the large-scale and steady surface uplift (at ~ 0.1
555 km/m.y) of the Eastern Cordillera and the Altiplano modeled by Sundell et al. (2019). These
556 values are too close from each other to identify each component. We can, however, say that
557 the area did experience surface uplift (Sundell et al., 2019), meaning that erosion had been
558 less important than rock uplift. The exhumation rates we obtained are the part of rock uplift
559 accommodated by erosion, while the remaining part (unconstrained by our
560 thermochronological record) was the surface uplift.

561 These observations are compatible with large-scale tectonic shortening (Lamb, 2011;
562 Phillips et al., 2012) and/or lower crustal flow (Husson and Sempere, 2003; Tassara, 2005;
563 Ouimet and Cook, 2010). We cannot, however, exclude more rapid surface uplift of the

564 northern Altiplano between 10 and 5 Ma (0.4 km/m.y as suggested by Kar et al., 2016).
565 Indeed, in a potentially endorheic context (Gérard et al., submitted), sediment evacuation and
566 thus large-scale erosion rates are low. Consequently, the Altiplano may have risen rapidly
567 without prominent incision and thus recorded limited exhumation (*i.e.* steady low exhumation
568 rates despite rapid surface uplift, as already indicated by our limited exhumation rates).
569 Nevertheless, it has been also demonstrated from regional-climate numerical modeling that
570 such a surface-uplift acceleration can be an artifact driven by the climatic variability (Ehlers
571 & Poulsen, 2009). We thus favor the conservative hypothesis of a steady, slow and
572 continuous surface uplift and low associated exhumation rates between 40 and 5 Ma. As a
573 result, and based on our thermochronological data, we also discard the potential implication
574 of one or multiple lithospheric delamination event(s) implying pulses of rapid surface uplift
575 during the Miocene (Garzione et al., 2017).

576

577 **5.3 Southern Eastern Cordillera – 5 Ma exhumation rate increase**

578 The southern Eastern Cordillera framed southward by the Apurimac fault system
579 registered an order-of-magnitude acceleration of exhumation since ~5 Ma, driven by both
580 topographic incision and tectonic uplift (this study; Gérard et al., submitted). The local 5-Ma
581 exhumation event affecting the southern Eastern Cordillera (Figure 12e) cannot be explained
582 by large-scale phenomenon such as lithospheric delamination, neither in terms of spatial
583 extent nor timing (Garzione et al., 2006; Sobolev and Babeyko, 2005). Only tectonic uplift
584 along local structures associated with erosion could explain our observed pattern of
585 thermochronological ages and exhumation (Figure 4, 6 and 7). Pecube inverse outcomes
586 show that the inherited crustal-scale Apurimac fault system can reproduce the 3D
587 thermochronological-data pattern, with significant tilting of the southern Eastern Cordillera
588 (Figure 10). In such a deflected thrusting pattern, it is geometrically difficult to link the

589 southern Eastern Cordillera to a ramp located beneath and connected to the Subandean front.
590 Furthermore, the Subandean front has been active since 14 Ma (Espurt et al., 2011), which
591 clearly predates the 5-Ma exhumation signal we observed in the Eastern Cordillera. The
592 Apurimac fault system appears to be the most likely structure tilting the Eastern Cordillera
593 (Figure 10) associated to backthrusting activity with a relatively low north-dipping angle of
594 30-40° (Figure 10d).

595 Considering end-member values of best-fit Pecube parameters (*i.e.* fault dipping
596 angle, timing for fault activation and fault velocity), we estimated total horizontal crustal
597 shortening ranging between 6 and 21 km (mean shortening rate of 2.8 ± 1.5 km/m.y.). The
598 total amount of vertical rock uplift ranges between 4 and 17 km (mean rock uplift rate of
599 2.2 ± 1.3 km/m.y.) since 5 Ma. The parameter ranges derived from our approach do not allow
600 to constrain precisely the tectonic deformation (nor vertical or horizontal) rates and thus to
601 further discriminate the tectonic balance and the respective importance of different rock uplift
602 drivers for the southern Eastern Cordillera. On the other hand, vertical tectonic uplift rates
603 overlap exhumation rates over the last 5 Ma (2.2 ± 1.3 km/m.y. vs. 1.2 ± 0.4 km/m.y.
604 respectively; Figure 11), which highlights the consistency between 2D and 3D modeling
605 approaches. Furthermore, constrained 5-Ma horizontal shortening rates for the southern
606 Eastern Cordillera (2.8 ± 1.5 km/m.y.) are also consistent with balanced cross-section
607 reconstructions and derived shortening rates in the Subandean area (~ 3.8 km/m.y.; Espurt et
608 al., 2011), directly located to the north of the Abancay Deflection (Figure 1).

609 Although thick-skinned backthrusts have been reported as active since the late-
610 Miocene to the north of the Abancay Deflection (Shira mountains; Gautheron et al., 2013;
611 Wimpenny et al., 2018; Huaytapallana fault, in the continuity of the Apurimac fault system;
612 Dorbath et al., 1990; Figure 3b), we document for the first time the recent tectonic activity
613 (*i.e.* <5 Ma) for the Abancay region itself, with significant but local exhumation through the

614 Apurimac fault system south-verging backthrusting. The low-magnitude earthquakes cluster
615 in this zone (Figure 3a) strongly corroborates our interpretation, also supporting the
616 hypothesis that such fault activity and observed exhumation pattern on million-year
617 timescales is still ongoing today.

618

619 **5.4 Potential drivers for the Apurimac fault system re-activation**

620 The Abancay Deflection is framed northward by the Subandean zone, which has been
621 tectonically active since ~14 Ma (Espurt et al., 2011). To the south, the Altiplano is
622 characterized by extensional faulting since the Quaternary (Sébrier et al., 1985; Wimpenny et
623 al., 2018). Our results show that the Eastern Cordillera was tilted through the south-verging
624 backthrust of the Apurimac fault system, which has been active since ~5 Ma (Figures 12e and
625 13). Considering the orogenic-prism balance theory (Whipple & Meade, 2004; Willett et al.,
626 1993), the tectonic-shortening transfer from the Altiplano to the Subandes (since ~15 Ma in
627 Bolivian Andes; Horton, 2005; Norton and Schlunegger, 2011; Anderson et al., 2018) was
628 triggered by sediment accumulation in the foreland basin (i.e. paleo-Subandean zone; Mosolf
629 et al., 2011) following the late-Miocene South-American monsoon intensification (Poulsen et
630 al., 2010). Thus, the question of the out-of-sequence Apurimac back thrust activity needs to
631 be addressed.

632 From a morphologic viewpoint, the peculiarity of the Abancay Deflection is that this
633 is the only region at the scale of the Altiplano where the hydrographic network is reaching
634 the core of the orogen after crossing the entire Eastern Cordillera (Apurimac and Urubamba
635 Rivers; Figures 1 and 12). The river capture, incision and subsequent increased denudation
636 was probably triggered and enhanced by wetter conditions during the late-Miocene (Poulsen
637 et al., 2010) and the Pliocene climate variability (Lease & Ehlers, 2013; Peizhen et al., 2001).
638 Given its reverse faulting timing initiation at ca. 5 Ma, the Apurimac fault system has played

639 as an out-of-sequence thrust. We thus conceptually interpret in the following the tectonic
640 evolution of the Abancay Deflection (Figures 12 and 13), linking the climate evolution and
641 the tectonic transfer regarding the orogenic prism rebalancing and geodynamic settings:

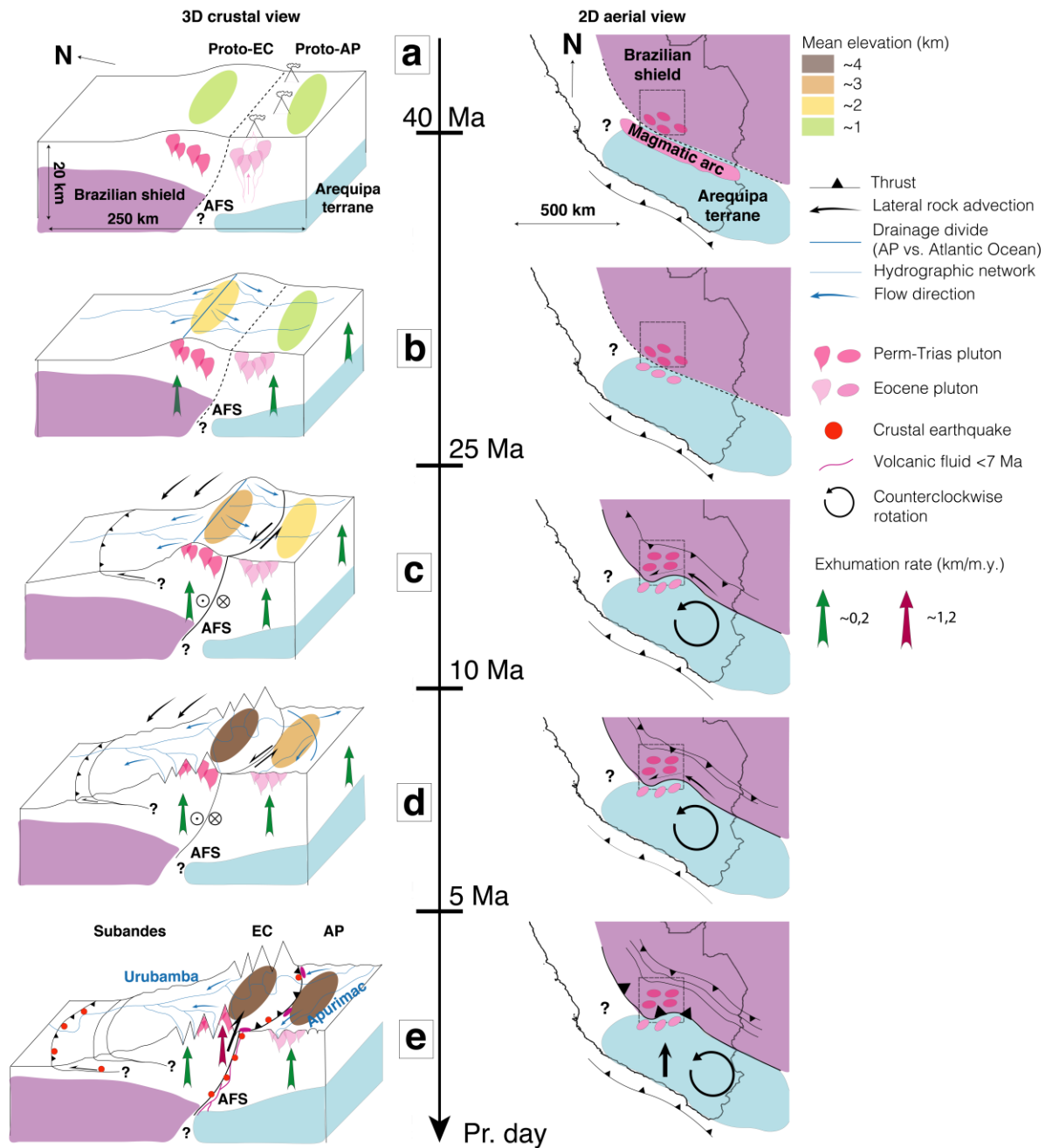
642 (1) Late-Miocene precipitation intensification (Poulsen et al., 2010) on the eastern
643 flank of the Peruvian Andes favored the regressive erosion through the proto-Apurimac and -
644 Urubamba Rivers. These paleo-drainage systems captured and incised the internally-drained
645 paleo-Abancay Deflection (Figures 12d and 12e).

646 (2) Consequently, this drainage capture and river incision subsequently enhanced
647 denudation processes over the large-scale Abancay Deflection. Rivers deeply carved the
648 Eastern Cordillera, sediments were exported toward the foreland basin and trapped within it
649 (paleo-Subandes).

650 (3) By orogenic prism rebalancing, the Subandean deformation propagated northward
651 at ~5 Ma (Mosolf et al., 2011; Gautheron et al., 2013). In the core of the orogen, mass
652 removal favored tectonically driven surface uplift of the eroding southern Eastern Cordillera
653 through the Apurimac fault system (Figures 12e and 13).

654 (4) Focused deformation localized on the Apurimac fault system may be explained by
655 its peculiar position at the northern edge of the Arequipa terrane (Figure 13; Loewy et al.,
656 2004). The south-verging Apurimac fault system plays the role of a buttress on which the
657 north-verging Subandean thrust ramp is rooted, forming a crustal-scale flower structure with
658 the underplated Arequipa terrane southward and the Brazilian shield northward (Figure 13).
659 The northward advance of the Arequipa terrane is still an ongoing process according to GPS
660 measures that favor the current Bolivian Orocline bending (Allmendinger et al., 2005).
661 Complementarily, the Apurimac fault system is a lithospheric-scale inherited structure
662 (Carlier et al., 2005; Dalmayrac et al., 1980; Sempere et al., 2002) and constitutes a
663 mechanical weak zone promoting the localization and accumulation of deformation.

664 Although the Andes present numerous deflected zones (*i.e.* Cajamarca, Huancabamba
665 in Peru; Dalmayrac et al., 1980), the Abancay Deflection is exceptional with respect to its
666 size, highly-rotated fault systems and its peculiar location at the northern tip of the Altiplano.
667 It marks abruptly the along-strike segmentation of the Central Andes facing the Amazonian
668 basin with E-W topographic high. Even if backthrusting activity through reactivated
669 Cretaceous crustal normal fault tilting in the Eastern Cordillera is already documented in
670 southern Peru (Perez et al., 2016), the Apurimac fault system backthrusting is abnormal and
671 unique. To our knowledge, there is nowhere else in the Andes a crustal-scale and even a
672 probable lithospheric-scale inherited structure (Carlier et al., 2005; Sempere et al., 2002) and
673 suture between the eastern Altiplano and the Eastern Cordillera reactivated as a backthrust
674 within the last 5 Ma providing stronger uplift in the Eastern Cordillera. The relative position
675 of the Arequipa terrane (Figure 12) acting as a rigid indenter (Gérard et al. submitted) could
676 explain the accumulation of horizontal and vertical deformation in such limited-extend area
677 and the subsequent orthogonal direction of the topography in comparison to the main orogen
678 elongation axis. This could furthermore explain this undocumented-before tectonic behavior
679 and probable higher erosion rates with an E-W topography facing the Amazonian moisture
680 flux enhancing orographic updraft.



681

682 **Figure 12.** Tectonomorphic evolution of the Abancay Deflection since 40 Ma. Right panels
 683 represent the large-scale schematic aerial views of the study area (black dashed square). Left
 684 panels are 3D Abancay Deflection schematic crustal blocks corresponding to the surface to
 685 the square defined in the right panels. a, b, c, d and e refer respectively to the situation at 40
 686 Ma, between 40 and 25 Ma, between 25 and 10 Ma, between 10 and 5 Ma and finally since 5
 687 Ma to present day. AFS: Apurimac fault system; EC: Eastern Cordillera; AP: Altiplano.

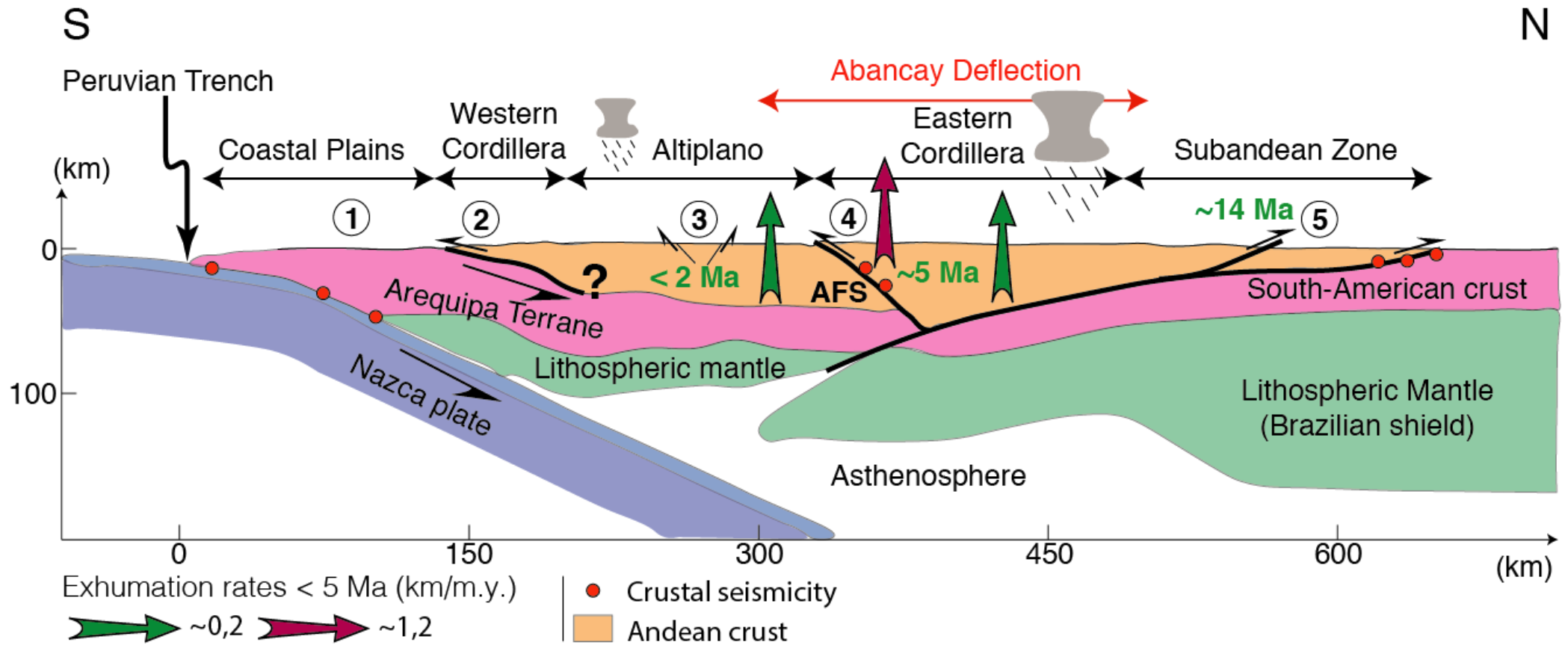


Figure 13. Andean orogenic model (South-North cross section) crossing through the Abancay Deflection since ca. 5 Ma. Modified after the double-verging prism orogenic model of Armijo et al. (2015). Green numbers refer to the initiation timing of the associated crustal deformation. Black circled numbers refer to the compiled previous and present studies: 1: Loewy et al. (2004); Ramos (2008, 2010); 2: Armijo et al. (2015); 3: Sébrier et al. (1985); Mercier et al. (1992); Wimpenny et al. (2018); 4: This study; 5: Espurt et al. (2011); Gautheron et al. (2013). AFS refers to Apurimac Fault System.

694 **5.5 Is the Abancay Deflection a Tectonic syntaxis?**

695 The Abancay Deflection presents numerous geomorphic, tectonic and geodynamic
696 features behind the theory of the tectonic syntaxes (Table 4) already documented in the
697 Himalaya (Namche Barwa; Nanga Parbat; e.g. Zeitler et al., 2001) and Alaska (Saint Elias
698 mount; e.g. Enkelmann et al., 2017). Focusing on the Abancay Deflection, high exhumation
699 rates concentrated in the core of a distorted zone of limited-extend and framed by deflected
700 active faults, promote the classification of the Abancay Deflection as a tectonic syntaxis
701 (This study; Table 4). In this case, the Arequipa terrane could play the role of the indenter in
702 response to counterclockwise rotation (Roperch et al., 2006) of the northern limb of the
703 Bolivian Orocline since the Miocene (Allmendinger et al., 2005; Müller et al., 2002).

704 The Himalayan syntaxes are characterized by heat advection, subsequent upward
705 deflection of isotherms inducing a brittle-ductile rheological limit to the ascent (Koons et al.,
706 2013). These peculiar thermal and rheological parameters associated to high geothermal
707 gradients ($\sim 60^{\circ}\text{C}/\text{km}$; Craw et al., 1994) and shallow seismicity ($\sim 2\text{-}5$ km depth; Meltzer et
708 al., 1998) are defining tectonic aneurisms (Koons et al., 2013). The Abancay Deflection,
709 however, seems to be relatively “cold” ($\sim 20^{\circ}\text{C}/\text{km}$; this study) and deeply brittle with poorly-
710 documented geothermal gradient measurements that rarely exceed $30^{\circ}\text{C}/\text{km}$ (Eastern
711 Cordillera far south in Bolivia; Barnes et al., 2008; Henry & Pollack, 1988), and up-to-30 km
712 crustal seismicity respectively (Figure 3a). Thus, the Abancay Deflection cannot be defined
713 as a tectonic aneurism.

714 The similarity in structural and geomorphic setting between the Abancay Deflection
715 and the Himalayan/Alaskan syntaxes, leads us to speculate that the Abancay Deflection may
716 reflect an incipient Andean syntaxis, where drainage capture and ensuing rapid incision of the
717 plateau edge led to focused exhumation and tectonic uplift along a deflected fault pattern. In
718 such a geodynamic context, associated to ocean – continent convergence, the closest

719 comparison can be done with the Denali syntaxis in Alaska (Figure 14). The Abancay
720 Deflection, however, do not reach yet (and maybe never) a mature stage of a tectonic
721 aneurism.

Table 4. Compilation of observations and comparison of documented tectonic syntaxes with the Abancay Deflection

Observation	Himalayan syntaxis	Alaskan syntaxis	Abancay Deflection
<u>Morphology</u>			
Positive anomaly of topography	YES Nanga Parbat mountains (NP) Namche Barwa mountains (NB) (Zeitler et al., 2001)	YES Denali mountains St Elias mount (Enkelmann et al., 2017)	YES Cordillera Vilcabamba (Salcantay, southern Eastern Cordillera) (Gérard et al. submitted)
High relief and incision	YES Indus River (NP) / Tsangpo River (NB) (Zeitler et al., 2001)	YES Seward et Logan glaciers (Enkelmann et al., 2017)	YES Urubamba River (Gérard et al. submitted)
Major crossing-orogens rivers	YES Indus River (NP) / Tsangpo River (NB) (Zeitler et al., 2001)	NA* Glaciated area	YES Urubamba River (This study; Gérard et al. submitted)
Captured high elevation plateau upstream	YES Tibetan plateau (Clark et al., 2004; Yang et al., 2016)	NO No plateau	YES Altiplano (This study; Gérard et al. submitted)

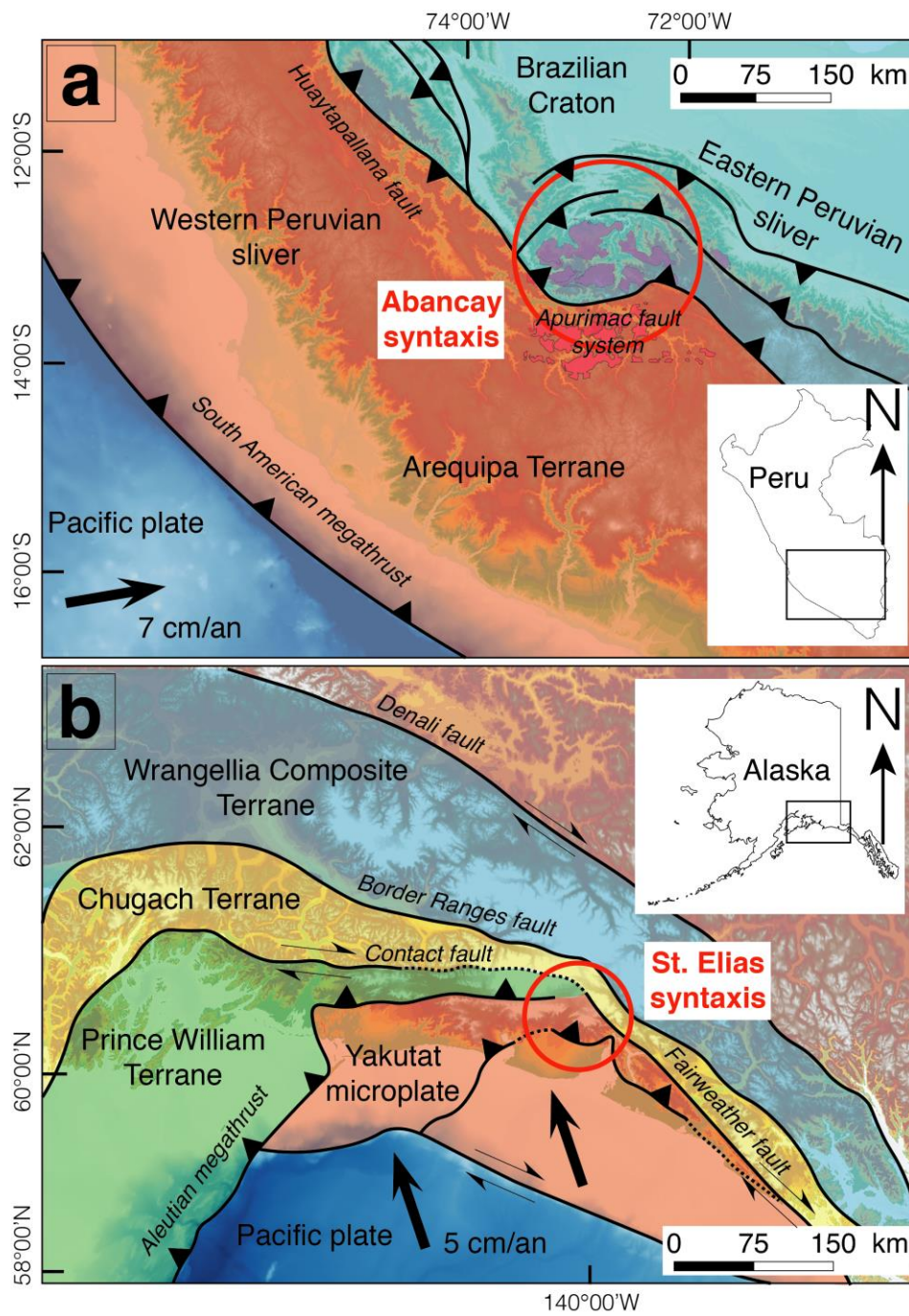
Observation	Himalayan syntaxis	Alaskan syntaxis	Abancay Deflection
Tightened and aligned rivers along active faults	YES Salween, Mekong / Yangtze Rivers (NB; Hallet & Molnar, 2001); Hari, Murgab et Helmand Rivers (NP; Brookfield, 1998)	NA* Glaciated area	YES Urubamba and Apurimac Rivers along the Apurimac fault system (This study; Gérard et al. submitted)
Knickpoints	YES Tsangpo River crossing the NB (Zeitler et al., 2001)	NA* Masked bedrock beneath the glaciers	YES Urubamba River crossing the Eastern Cordillera (Gérard et al. submitted)
<u>Tectonics and Geodynamic</u>			
Tectonic rotation and strike-slip faulting	YES Crustal folding through orogen-parallel compression (Royden et al., 1997) Jiali-Parlung fault (NB; Burg et al., 1998) Karakorum fault (NP; Bossart et al., 1988)	YES Fairweather fault (Chapman et al., 2012)	YES Counterclockwise rotation and left-lateral component of the Apurimac fault during Miocene (Dalmayrac et al., 1980; Roperch et al., 2006)
Thick-skinned tectonic	YES (Zeitler et al., 2001)	YES (Chapman et al., 2012)	YES Apurimac fault delimiting 2 crustal blocks (This study; Carlier et al., 2005)

Observation	Himalayan syntaxis	Alaskan syntaxis	Abancay Deflection
Localized deformation	YES	YES	YES
along crustal-scale faults and magmatic fluid circulation	(NP; Edwards et al., 2000; Schneider et al., 1999; Seeber & Pêcher, 1998)	Except for fluids circulation (Koons et al., 2010, 2013)	Apurimac fault and volcanic fluids circulation since ~7 Ma (Carlier et al., 1996; Carlier et al., 2005)
Indenter	YES	YES	YES
	Indian plate (Burtman & Molnar, 1993)	Yakutat terrane (Koons et al., 2010; Marechal et al., 2015)	Arequipa terrane (Ramos, 2010; Villegas-Lanza et al., 2016)
Higher exhumation rates into the core of the syntaxis	YES	YES	YES
	~10 km/m.y. since ~1 Ma (King et al., 2016)	~2 to ~5 km/m.y. since ~2 Ma (Enkelmann et al., 2009; Enkelmann et al., 2017; Falkowski et al., 2014)	~1,2 km/m.y. since ~5 Ma (This study)
<u>Conclusion</u>			
Tectonic syntaxis	YES	YES	YES
*Not applicable			

723

724

725



726

727 **Figure 14.** Geodynamic comparison between the Abancay Deflection and the St. Elias
 728 syntaxis of Alaska. a) The Abancay Deflection case; the bulls-eye structure and morphology
 729 of the Abancay Deflection (red circle) suggests that it is an incipient syntaxis, with the
 730 Arequipa terrane acting as the indenter. b) The St. Elias case from Falkowski et al. (2014).
 731 The Yakutat microplate plays the role of the indenter for this Alaskan syntaxis.

732 6 Conclusions

733 Our new thermochronological data and inverse thermo(-kinematic) modeling from the
734 Abancay Deflection reveal steady and spatially-uniform exhumation for the whole study area
735 between 40 and 5 Ma, at a moderate rate of ~ 0.2 km/m.y. We interpret the exhumation rate as
736 evidence for large-scale crustal shortening and/or lower crustal flow associated to low-
737 magnitude erosion rates in an internally-drained area. The differential exhumation of the
738 Abancay Deflection area initiated at ~ 5 Ma, characterized by $\sim 500\%$ increase in exhumation
739 rate for the southern Eastern Cordillera (~ 1.2 km/m.y). This 5-Ma exhumation signal has
740 been driven by incision (capture of the paleo-endoreic environment) and enhanced by
741 tectonically driven rock uplift through the Apurimac fault system activation as a south-
742 verging backthrust. For the first time, we document the recent (< 5 Ma) and ongoing tectonic
743 activity of this fault system. Finally, we propose the late-Miocene precipitation intensification
744 and the Arequipa terrane underplating as potential triggers for the re-activation of this out-of-
745 sequence inherited crustal-scale thrust. Considering such a geomorphic and structural setting
746 together with rapid and focused exhumation, in a region of anomalously high relief and
747 topography, we speculate that the Abancay Deflection may represent the first identified
748 incipient Andean syntaxis.

749

750 Acknowledgements

751 This work was supported by the IRD (Institut de Recherche pour le Développement),
752 ISTERre, the INSU (Institut National des Sciences de l'Univers), and the ANR-12-NS06-
753 0005-01 project for the AHe analysis. We are grateful to the SERNANP, the INGEMMET
754 (Cusco-PATA convenio 006-2016-Fondecyt) and the National Archaeological Park of Machu
755 Picchu, for the provided facilities. We thank P.H. Leloup and G. Mahéo (Géode laboratory,
756 Lyon) and the GTC platform (F. Coeur & F. Sénebier, ISTERre, Grenoble) for sample

757 processing, as well as M. Balvay, R. Pinna-Jamme & F. Haurine for assistance during AFT
758 and AHe dating. Datasets for this research are included in this paper (and its supplementary
759 information files).

760

761 **References**

762 Allmendinger, R. W., Smalley, R., Bevis, M., Caprio, H., & Brooks, B. (2005). Bending the
763 Bolivian orocline in real time. *Geology*, *33*(11), 905–908.

764 <https://doi.org/10.1130/G21779.1>

765 Anderson, R. B., Long, S. P., Horton, B. K., Thomson, S. N., Calle, A. Z., & Stockli, D. F.
766 (2018). Orogenic Wedge Evolution of the Central Andes, Bolivia (21°S): Implications
767 for Cordilleran Cyclicity. *Tectonics*, *37*(10), 3577–3609.

768 <https://doi.org/10.1029/2018TC005132>

769 Armijo, R., Lacassin, R., Coudurier-Curveur, A., & Carrizo, D. (2015). Coupled tectonic
770 evolution of Andean orogeny and global climate. *Earth-Science Reviews*. Elsevier B.V.

771 <https://doi.org/10.1016/j.earscirev.2015.01.005>

772 Arndt, J., Bartel, T., Scheuber, E., & Schilling, F. (1997). Thermal and rheological properties
773 of granodioritic rocks from the Central Andes, North Chile. *Tectonophysics*, *271*(1–2),

774 75–88. [https://doi.org/10.1016/S0040-1951\(96\)00218-1](https://doi.org/10.1016/S0040-1951(96)00218-1)

775 Ault, A. K., Gautheron, C., & King, G. E. (2019). Innovations in (U-Th)/He, fission-track,
776 and trapped-charge thermochronometry with applications to earthquakes, weathering,
777 surface-mantle connections, and the growth and decay of mountains. *Tectonics*.

778 <https://doi.org/10.1029/2018tc005312>

779 Barnes, J B, & Ehlers, T. A. (2009). End member models for Andean Plateau uplift. *Earth-*
780 *Science Reviews*. Elsevier B.V. <https://doi.org/10.1016/j.earscirev.2009.08.003>

781 Barnes, Jason B., Ehlers, T. A., Insel, N., McQuarrie, N., & Poulsen, C. J. (2012). Linking

- 782 orography, climate, and exhumation across the central Andes. *Geology*, 40(12), 1135–
783 1138. <https://doi.org/10.1130/G33229.1>
- 784 Barnes, Jason B, Ehlers, T. A., McQuarrie, N., O’Sullivan, P. B., & Tawackoli, S. (2008).
785 Thermochronometer record of central Andean Plateau growth, Bolivia (19.5°S).
786 *Tectonics*, 27(3). <https://doi.org/10.1029/2007TC002174>
- 787 Bonhomme, M., Fornari, M., Laubacher, G., Sébrier, M., & Vivier, G. (1988). New Cenozoic
788 K-Ar ages on volcanic rocks from the eastern High Andes, southern Peru. *Journal of*
789 *South American Earth Sciences*, 1(2), 179–183.
- 790 Bossart, P., Dietrich, D., Greco, A., Ottiger, R., & Ramsay, J. (1988). The Tectonic Structure
791 of the Hazara-Kashmir Syntaxis, Southern Himalayas, Pakistan. *Tectonics*, 7(2), 273–
792 297.
- 793 Braun, J. (2003). Pecube: A new finite-element code to solve the 3D heat transport equation
794 including the effects of a time-varying, finite amplitude surface topography. *Computers*
795 *and Geosciences*, 29(6), 787–794. [https://doi.org/10.1016/S0098-3004\(03\)00052-9](https://doi.org/10.1016/S0098-3004(03)00052-9)
- 796 Braun, J., van der Beek, P., Valla, P., Robert, X., Herman, F., Glotzbach, C., et al. (2012).
797 Quantifying rates of landscape evolution and tectonic processes by thermochronology
798 and numerical modeling of crustal heat transport using PECUBE. *Tectonophysics*, 524–
799 525, 1–28. <https://doi.org/10.1016/j.tecto.2011.12.035>
- 800 Brookfield, M. E. (1998). The evolution of the great river systems of southern Asia during
801 the Cenozoic India-Asia collision: rivers draining southwards. *Geomorphology*, 22(3–4),
802 285–312. [https://doi.org/10.1016/S0169-555X\(97\)00082-2](https://doi.org/10.1016/S0169-555X(97)00082-2)
- 803 Brown, R. W., Beucher, R., Roper, S., Persano, C., Stuart, F., & Fitzgerald, P. (2013).
804 Natural age dispersion arising from the analysis of broken crystals. Part I: Theoretical
805 basis and implications for the apatite (U-Th)/He thermochronometer. *Geochimica et*
806 *Cosmochimica Acta*, 122(120), 478–497. <https://doi.org/10.1016/j.gca.2013.05.041>

- 807 Burg, J. P., Nievergelt, P., Oberli, F., Seward, D., Davy, P., Maurin, J. C., et al. (1998). The
808 Namche Barwa syntaxis: Evidence for exhumation related to compressional crustal
809 folding. *Journal of Asian Earth Sciences*, *16*(2–3), 239–252.
810 [https://doi.org/10.1016/S0743-9547\(98\)00002-6](https://doi.org/10.1016/S0743-9547(98)00002-6)
- 811 Burtman, V., & Molnar, P. (1993). Geological and geophysical evidence for deep subduction
812 of continental crust beneath the Pamir. *Geological Society of America Special Paper*,
813 *281*, 1–76.
- 814 Cabrera, J., Sébrier, M., & Mercier, J. L. (1991). Plio-Quaternary geodynamic evolution of a
815 segment of the Peruvian Andean Cordillera located above the change in the subduction
816 geometry: the Cuzco region. *Tectonophysics*, *190*(2–4), 331–362.
817 [https://doi.org/10.1016/0040-1951\(91\)90437-W](https://doi.org/10.1016/0040-1951(91)90437-W)
- 818 Carlier, G, Lorand, J. P., Bonhomme, M., & Carlotto, V. (1996). A reappraisal of the
819 cenozoic inner arc magmatism in southern Peru: consequences for the evolution of the
820 central Andes for the past 50 Ma. *Third ISAG*, (January), 551–554.
- 821 Carlier, Gabi, Lorand, J. P., Liégeois, J. P., Fornari, M., Soler, P., Carlotto, V., & Cárdenas, J.
822 (2005). Potassic-ultrapotassic mafic rocks delineate two lithospheric mantle blocks
823 beneath the southern Peruvian Altiplano. *Geology*, *33*(7), 601–604.
824 <https://doi.org/10.1130/G21643.1>
- 825 Carlotto, V. (2013). Paleogeographic and tectonic controls on the evolution of Cenozoic
826 basins in the Altiplano and Western Cordillera of southern Peru. *Tectonophysics*, *589*,
827 195–219. <https://doi.org/10.1016/j.tecto.2013.01.002>
- 828 Chapman, J. B., Pavlis, T. L., Bruhn, R. L., Worthington, L. L., Gulick, S. P. S., & Berger, A.
829 L. (2012). Structural relationships in the eastern syntaxis of the St. Elias orogen, Alaska.
830 *Geosphere*, *8*(1), 105–126. <https://doi.org/10.1130/GES00677.1>
- 831 Clark, M. K., Schoenbohm, L. M., Royden, L. H., Whipple, K. X., Burchfiel, B. C., Zhang,

- 832 X., et al. (2004). Surface uplift, tectonics, and erosion of eastern Tibet from large-scale
833 drainage patterns. *Tectonics*, 23(1), 1–21. <https://doi.org/10.1029/2002TC001402>
- 834 Craw, D., Koons, P. O., Winslow, D., Chamberlain, C. P., & Zeitler, P. (1994). Boiling fluids
835 in a region of rapid uplift, Nanga Parbat Massif, Pakistan. *Earth and Planetary Science*
836 *Letters*, 128(3–4), 169–182. [https://doi.org/10.1016/0012-821X\(94\)90143-0](https://doi.org/10.1016/0012-821X(94)90143-0)
- 837 Dalmayrac, B., Laubacher, G., & Marocco, R. (1980). *Géologie des Andes péruviennes*
838 (ORSTOM). Paris.
- 839 Dorbath, C., Dorbath, L., Cisternas, A., Deverchére, J., & Sebrier, M. (1990). Seismicity of
840 the huancayo basin (central Peru) and the huaytapallana fault. *Journal of South*
841 *American Earth Sciences*, 3(1), 21–29. [https://doi.org/10.1016/0895-9811\(90\)90015-S](https://doi.org/10.1016/0895-9811(90)90015-S)
- 842 Dziewonski, A. M., Chou, T. A., & Woodhouse, J. H. (1981). Determination of earthquake
843 source parameters from waveform data for studies of global and regional seismicity.
844 *Journal of Geophysical Research*, 86(B4), 2825–2852.
845 <https://doi.org/10.1029/JB086iB04p02825>
- 846 Edwards, M. A., Kidd, W. S. F., Khan, M. A., & Schneider, D. A. (2000). Tectonics of the
847 SW margin of the Nanga Parbat-Haramosh massif. *Geological Society, London, Special*
848 *Publications*, (170), 77–100.
- 849 Egeler, C., & De Booy, T. (1961). Preliminary Note on the Geology of the Cordillera
850 Vilcabamba (SE Peru), with Emphasis on the... *Geologie & Mijnbouw*, 40(3), 319–325.
- 851 Ehlers, T. A., Chaudhri, T., Kumar, S., Fuller, C. W., Willett, S. D., Ketcham, R. A., &
852 Brandon, M. T. (2005). Computational Tools for Low-Temperature Thermochronometer
853 Interpretation. *Reviews in Mineralogy and Geochemistry*, 58(1), 589–622.
854 <https://doi.org/10.2138/rmg.2005.58.22>
- 855 Ehlers, Todd A., & Poulsen, C. J. (2009). Influence of Andean uplift on climate and
856 paleoaltimetry estimates. *Earth and Planetary Science Letters*, 281(3–4), 238–248.

- 857 <https://doi.org/10.1016/j.epsl.2009.02.026>
- 858 Ekström, G., Nettles, M., & Dziewoński, A. M. (2012). The global CMT project 2004-2010:
859 Centroid-moment tensors for 13,017 earthquakes. *Physics of the Earth and Planetary*
860 *Interiors*, 200–201, 1–9. <https://doi.org/10.1016/j.pepi.2012.04.002>
- 861 Enkelmann, E., Zeitler, P. K., Pavlis, T. L., Garver, J. I., & Ridgway, K. D. (2009). Intense
862 localized rock uplift and erosion in the StElias orogen of Alaska. *Nature Geoscience*,
863 2(5), 360–363. <https://doi.org/10.1038/ngeo502>
- 864 Enkelmann, Eva, Piestrzeniewicz, A., Falkowski, S., Stübner, K., & Ehlers, T. A. (2017).
865 Thermochronology in southeast Alaska and southwest Yukon: Implications for North
866 American Plate response to terrane accretion. *Earth and Planetary Science Letters*, 457,
867 348–358. <https://doi.org/10.1016/j.epsl.2016.10.032>
- 868 Espurt, N., Barbarand, J., Roddaz, M., Brusset, S., Baby, P., Saillard, M., & Hermoza, W.
869 (2011). A scenario for late Neogene Andean shortening transfer in the Camisea
870 Subandean zone (Peru, 12°S): Implications for growth of the northern Andean Plateau.
871 *Bulletin of the Geological Society of America*, 123(9–10), 2050–2068.
872 <https://doi.org/10.1130/B30165.1>
- 873 Evans, N. J., Byrne, J. P., Keegan, J. T., & Dotter, L. E. (2005). Determination of Uranium
874 and Thorium in Zircon, Apatite, and Fluorite: Application to Laser (U–Th)/He
875 Thermochronology. *Journal of Analytical Chemistry*, 60(12), 1159–1165.
- 876 Falkowski, S., Enkelmann, E., & Ehlers, T. A. (2014). Constraining the area of rapid and
877 deep-seated exhumation at the St. Elias syntaxis, Southeast Alaska, with detrital zircon
878 fission-track analysis. *Tectonics*, 33(5), 597–616.
879 <https://doi.org/10.1002/2013TC003408>
- 880 Farley, K A. (2000). Helium diffusion from apatite: General behavior as illustrated by
881 Durango fluorapatite. *Journal of Geophysical Research: Solid Earth*, 105(B2), 2903–

- 882 2914. <https://doi.org/10.1029/1999jb900348>
- 883 Farley, Kenneth A. (2002). (U-Th)/He Dating: Techniques, Calibrations, and Applications.
884 *Reviews in Mineralogy and Geochemistry*, 47, 819–844.
885 <https://doi.org/10.2138/rmg.2002.47.18>
- 886 Galbraith, R. F., & Laslett, G. M. (1993). Statistical models for mixed fission track ages.
887 *International Journal of Radiation Applications and Instrumentation. Part*, 21(4), 459–
888 470. [https://doi.org/10.1016/1359-0189\(93\)90185-C](https://doi.org/10.1016/1359-0189(93)90185-C)
- 889 Gallagher, K. (2012). Transdimensional inverse thermal history modeling for quantitative
890 thermochronology. *Journal of Geophysical Research: Solid Earth*, 117(2), 1–16.
891 <https://doi.org/10.1029/2011JB008825>
- 892 Garzione, C. N., Molnar, P., Libarkin, J. C., & MacFadden, B. J. (2006). Rapid late Miocene
893 rise of the Bolivian Altiplano: Evidence for removal of mantle lithosphere. *Earth and*
894 *Planetary Science Letters*, 241(3–4), 543–556.
895 <https://doi.org/10.1016/j.epsl.2005.11.026>
- 896 Garzione, C. N., McQuarrie, N., Perez, N. D., Ehlers, T. A., Beck, S. L., Kar, N., et al.
897 (2017). Tectonic Evolution of the Central Andean Plateau and Implications for the
898 Growth of Plateaus. *Annual Review of Earth and Planetary Sciences*, 45(1), 529–559.
899 <https://doi.org/10.1146/annurev-earth-063016-020612>
- 900 Gautheron, C., & Tassan-Got, L. (2010). A Monte Carlo approach to diffusion applied to
901 noble gas/helium thermochronology. *Chemical Geology*, 273(3–4), 212–224.
902 <https://doi.org/10.1016/j.chemgeo.2010.02.023>
- 903 Gautheron, C., Tassan-Got, L., Barbarand, J., & Pagel, M. (2009). Effect of alpha-damage
904 annealing on apatite (U-Th)/He thermochronology. *Chemical Geology*, 266(3–4), 166–
905 179. <https://doi.org/10.1016/j.chemgeo.2009.06.001>
- 906 Gautheron, C., Tassan-Got, L., Ketcham, R. A., & Dobson, K. J. (2012). Accounting for long

- 907 alpha-particle stopping distances in (U-Th-Sm)/He geochronology: 3D modeling of
908 diffusion, zoning, implantation, and abrasion. *Geochimica et Cosmochimica Acta*, 96,
909 44–56. <https://doi.org/10.1016/j.gca.2012.08.016>
- 910 Gautheron, C., Espurt, N., Barbarand, J., Roddaz, M., Baby, P., Brusset, S., et al. (2013).
911 Direct dating of thick- and thin-skin thrusts in the Peruvian Subandean zone through
912 apatite (U-Th)/He and fission track thermochronometry. *Basin Research*, 25(4), 419–
913 435. <https://doi.org/10.1111/bre.12012>
- 914 Glotzbach, C., van der Beek, P. A., & Spiegel, C. (2011). Episodic exhumation and relief
915 growth in the Mont Blanc massif, Western Alps from numerical modelling of
916 thermochronology data. *Earth and Planetary Science Letters*, 304(3–4), 417–430.
917 <https://doi.org/10.1016/j.epsl.2011.02.020>
- 918 Gonfiantini, R., Roche, M.-A., Olivry, J.-C., Fontes, J.-C., & Zuppi, G. M. (2001). The
919 altitude effect on the isotopic composition of tropical rains. *Chemical Geology*, (181),
920 147–167.
- 921 Gotberg, N., McQuarrie, N., & Caillaux, V. C. (2010). Comparison of crustal thickening
922 budget and shortening estimates in southern Peru (12–14°S): Implications for mass
923 balance and rotations in the “Bolivian orocline.” *Bulletin of the Geological Society of*
924 *America*, 122(5–6), 727–742. <https://doi.org/10.1130/B26477.1>
- 925 Green, P. F. (1981). A new look at statistics in fission-track dating. *Nuclear Tracks*, 5, 77–86.
- 926 Hallet, B., & Molnar, P. (2001). Distorted drainage basins as markers of crustal strain east of
927 the Himalaya. *Journal of Geophysical Research: Solid Earth*, 106(B7), 13697–13709.
928 <https://doi.org/10.1029/2000jb900335>
- 929 Henry, S., & Pollack, H. (1988). Terrestrial Heat Flow Above the Andean Subduction Zone
930 in Bolivia and Peru. *Journal of Geophysical Research*, 93(B12), 153–162.
931 <https://doi.org/10.1029/JB093iB12p15153>

- 932 Horton, B. K. (2005). Revised deformation history of the central Andes: Inferences from
933 Cenozoic foredeep and intermontane basins of the Eastern Cordillera, Bolivia.
934 *Tectonics*. <https://doi.org/10.1029/2003TC001619>
- 935 Horton, B. K., Perez, N. D., Fitch, J. D., & Saylor, J. E. (2014). Punctuated shortening and
936 subsidence in the Altiplano Plateau of southern Peru: Implications for early Andean
937 mountain building. *Lithosphere*, 7(2), 117–137. <https://doi.org/10.1130/L397.1>
- 938 Husson, L., & Sempere, T. (2003). Thickening the Altiplano crust by gravity-driven crustal
939 channel flow. *Geophysical Research Letters*, 30(5), 1–4.
940 <https://doi.org/10.1029/2002GL016877>
- 941 Insel, N., Poulsen, C. J., & Ehlers, T. A. (2010). Influence of the Andes Mountains on South
942 American moisture transport, convection, and precipitation. *Climate Dynamics*, 35(7),
943 1477–1492. <https://doi.org/10.1007/s00382-009-0637-1>
- 944 Jaillard, E., & Soler, P. (1996). Cretaceous to early Paleogene tectonic evolution of the
945 northern Central Andes (0-18 degrees S) and its relations to geodynamics.
946 *Tectonophysics*, 259(2), 41–53. [https://doi.org/10.1016/0040-1951\(95\)00107-7](https://doi.org/10.1016/0040-1951(95)00107-7)
- 947 Kar, N., Garzzone, C. N., Jaramillo, C., Shanahan, T., Carlotto, V., Pullen, A., et al. (2016).
948 Rapid regional surface uplift of the northern Altiplano plateau revealed by multiproxy
949 paleoclimate reconstruction. *Earth and Planetary Science Letters*, 447, 33–47.
950 <https://doi.org/10.1016/j.epsl.2016.04.025>
- 951 Kennan, L. (2008). Fission track ages and sedimentary provenance studies in Peru, and their
952 implications for andean paleogeographic evolution, stratigraphy and hydrocarbon
953 systems. *VI INGEPET*. Retrieved from
954 <http://www.agu.org/pubs/crossref/1988/JB093iB12p15153.shtml>
- 955 Ketcham, R. A., Donelick, R. A., & Carlson, W. D. (1999). Variability of apatite fission-
956 track annealing kinetics: III. Crystallographic orientation effects. *American*

- 957 *Mineralogist*, 84, 1235–1255. <https://doi.org/10.2138/am-1999-0902>
- 958 Ketcham, R. A., Carter, A., Donelick, R. A., Barbarand, J., & Hurford, A. J. (2007).
959 Improved modeling of fission-track annealing in apatite. *American Mineralogist*, 92(5–
960 6), 799–810. <https://doi.org/10.2138/am.2007.2281>
- 961 Ketcham, R. A., Gautheron, C., & Tassan-Got, L. (2011). Accounting for long alpha-particle
962 stopping distances in (U-Th-Sm)/He geochronology: Refinement of the baseline case.
963 *Geochimica et Cosmochimica Acta*, 75(24), 7779–7791.
964 <https://doi.org/10.1016/j.gca.2011.10.011>
- 965 King, G. E., Herman, F., & Guralnik, B. (2016). Northward migration of the eastern
966 Himalayan syntaxis revealed by OSL thermochronometry. *Science*, 353(6301), 800–
967 804. <https://doi.org/10.1126/science.aaf2637>
- 968 Koons, P. O., Hooks, B. P., Pavlis, T., Upton, P., & Barker, A. D. (2010). Three-dimensional
969 mechanics of Yakutat convergence in the southern Alaskan plate corner. *Tectonics*,
970 29(4), 1–17. <https://doi.org/10.1029/2009TC002463>
- 971 Koons, P. O., Zeitler, P. K., & Hallet, B. (2013). Tectonic Aneurysms and Mountain
972 Building. In *Treatise on Geomorphology* (Vol. 5, pp. 318–349).
973 <https://doi.org/10.1016/B978-0-12-374739-6.00094-4>
- 974 Lamb, S. (2011). Did shortening in thick crust cause rapid Late Cenozoic uplift in the
975 northern Bolivian Andes? *Journal of the Geological Society*, 168(5), 1079–1092.
976 <https://doi.org/10.1144/0016-76492011-008>
- 977 Lancelot, J. R., Laubacher, G., Marocco, R., & Renaud, U. (1978). U/Pb radiochronology of
978 two granitic plutons from the eastern Cordillera (Peru) - Extent of Permian magmatic
979 activity and consequences. *Geologische Rundschau*, 67(1), 236–243.
980 <https://doi.org/10.1007/BF01803263>
- 981 Lease, R. O., & Ehlers, T. A. (2013). Incision into the eastern Andean Plateau during

- 982 Pliocene cooling. *Science*, 341(6147), 774–776. <https://doi.org/10.1126/science.1239132>
- 983 Loewy, S. L., Connelly, J. N., & Dalziel, I. W. D. (2004). An orphaned basement block: The
984 Arequipa-Antofalla Basement of the central Andean margin of South America. *Bulletin*
985 *of the Geological Society of America*, 116(1–2), 171–187.
986 <https://doi.org/10.1130/B25226.1>
- 987 Mamani, M., Wörner, G., & Sempere, T. (2010). Geochemical variations in igneous rocks of
988 the Central Andean orocline (13°S to 18°S): Tracing crustal thickening and magma
989 generation through time and space. *Bulletin of the Geological Society of America*,
990 122(1–2), 162–182. <https://doi.org/10.1130/B26538.1>
- 991 Marechal, A., Mazzotti, S., Elliott, J., Freymueller, J., & Schmidt, M. (2015). Indentor-corner
992 tectonics in the Yakutat-St. Elias collision constrained by GPS. *Journal of Geophysical*
993 *Research: Solid Earth*, 120, 3897–3908.
994 <https://doi.org/10.1002/2015JB012608>.Received
- 995 Marocco, R. (1971). Etude géologique de la chaîne andine au niveau de la déflexion
996 d'Abancay (Pérou). *Cah. ORSTOM*, (1971), 45–58.
- 997 Meltzer, A. S., Sarker, G. L., Seeber, L., & Armbruster, J. (1998). Snap, crackle, pop!
998 Seismicity and crustal structure at Nanga Parbat, Pakistan, Himalaya. *Eos (Transactions,*
999 *American Geophysical Union*, 79(F909).
- 1000 Mercier, L., Sébrier, M., Lavenu, A., Cabrera, J., Bellier, O., Dumont, J. ., & Machare, J.
1001 (1992). Changes in the Tectonic Regime Above a Subduction Zone of Andean Type:
1002 The Andes of Peru and Bolivia During the Pliocene-Pleistocene. *Journal of Geophysical*
1003 *Research*, 97(B8), 945–982.
- 1004 Mišković, A., Spikings, R. A., Chew, D. M., Košler, J., Ulianov, A., & Schaltegger, U.
1005 (2009). Tectonomagmatic evolution of Western Amazonia: Geochemical
1006 characterization and zircon U-Pb geochronologic constraints from the Peruvian Eastern

- 1007 Cordilleran granitoids. *Bulletin of the Geological Society of America*, 121(9–10), 1298–
1008 1324. <https://doi.org/10.1130/B26488.1>
- 1009 Mosolf, J. G., Horton, B. K., Heizler, M. T., & Matos, R. (2011). Unroofing the core of the
1010 central Andean fold-thrust belt during focused late Miocene exhumation: Evidence from
1011 the Tipuani-Mapiri wedge-top basin, Bolivia. *Basin Research*, 23(3), 346–360.
1012 <https://doi.org/10.1111/j.1365-2117.2010.00491.x>
- 1013 Müller, J. P., Kley, J., & Jacobshagen, V. (2002). Structure and Cenozoic kinematics of the
1014 Eastern Cordillera, southern Bolivia (21°S). *Tectonics*, 21(5), 1-1-1–24.
1015 <https://doi.org/10.1029/2001tc001340>
- 1016 Norton, K., & Schlunegger, F. (2011). Migrating deformation in the Central Andes from
1017 enhanced orographic rainfall. *Nature Communications*, 2(1).
1018 <https://doi.org/10.1038/ncomms1590>
- 1019 Ouimet, W. B., & Cook, K. L. (2010). Building the central Andes through axial lower crustal
1020 flow. *Tectonics*, 29(3), 1–15. <https://doi.org/10.1029/2009TC002460>
- 1021 Peizhen, Z., Molnar, P., & Downs, W. R. (2001). Increased sedimentation rates and grain
1022 sizes 2-4 Ma ago due to the influence of climate change on erosion rates. *Nature*,
1023 410(April), 891–897.
1024 https://doi.org/http://www.nature.com/nature/journal/v410/n6831/supinfo/410891a0_S
1025 1.html
- 1026 Perello, J., Carlotto, V., Zarate, A., Ramos, P., Posso, H., Neyra, C., et al. (2003). Porphyry-
1027 Style Alteration and Mineralization of the Middle Eocene to Early Oligocene
1028 Andahuaylas-Yauri Belt , Cuzco Region , Peru. *Economic Geology*, 98, 1575–1605.
- 1029 Perez, N. D., Horton, B. K., & Carlotto, V. (2016). Structural inheritance and selective
1030 reactivation in the central Andes: Cenozoic deformation guided by pre-Andean
1031 structures in southern Peru. *Tectonophysics*, 671, 264–280.

- 1032 <https://doi.org/10.1016/j.tecto.2015.12.031>
- 1033 Phillips, K., Clayton, R. W., Davis, P., Tavera, H., Guy, R., Skinner, S., et al. (2012).
1034 Structure of the subduction system in southern Peru from seismic array data. *Journal of*
1035 *Geophysical Research*, 117(11), 1–17. <https://doi.org/10.1029/2012JB009540>
- 1036 Poulsen, C. J., Ehlers, T. A., & Insel, N. (2010). Onset of Convective Rainfall During
1037 Gradual Late Miocene Rise of the Central Andes. *Science*, 328(April), 490–494.
1038 <https://doi.org/10.1126/science.1185078>
- 1039 Rak, A. J., McQuarrie, N., & Ehlers, T. A. (2017). Kinematics, Exhumation, and
1040 Sedimentation of the North Central Andes (Bolivia): An Integrated Thermochronometer
1041 and Thermokinematic Modeling Approach. *Tectonics*, 36(11), 2524–2554.
1042 <https://doi.org/10.1002/2016TC004440>
- 1043 Ramos, V. A. (2008). The Basement of the Central Andes: The Arequipa and Related
1044 Terranes. *Annual Review of Earth and Planetary Sciences*, 36(1), 289–324.
1045 <https://doi.org/10.1146/annurev.earth.36.031207.124304>
- 1046 Ramos, V. A. (2010). The Grenville-age basement of the Andes. *Journal of South American*
1047 *Earth Sciences*, 29(1), 77–91. <https://doi.org/10.1016/j.jsames.2009.09.004>
- 1048 Recanati, A., Gautheron, C., Barbarand, J., Missenard, Y., Pinna-Jamme, R., Tassan-Got, L.,
1049 et al. (2017). Helium trapping in apatite damage: Insights from (U-Th-Sm)/He dating of
1050 different granitoid lithologies. *Chemical Geology*, 470(September), 116–131.
1051 <https://doi.org/10.1016/j.chemgeo.2017.09.002>
- 1052 Reiners, P. W., & Brandon, M. T. (2006). Using Thermochronology To Understand Orogenic
1053 Erosion. *Annual Review of Earth and Planetary Sciences*, 34(1), 419–466.
1054 <https://doi.org/10.1146/annurev.earth.34.031405.125202>
- 1055 Reiners, P. W., & Shuster, D. L. (2009). Thermochronology and landscape evolution. *Physics*
1056 *Today*, (September), 31–36.

- 1057 Reitsma, M. J. (2012). *Reconstructing the Late Paleozoic - Early Mesozoic plutonic and*
1058 *sedimentary record of south-east Peru : Orphaned back-arcs along the western margin*
1059 *of Gondwana.*
- 1060 Robert, X., Van Der Beek, P., Braun, J., Perry, C., & Mugnier, J. L. (2011). Control of
1061 detachment geometry on lateral variations in exhumation rates in the Himalaya: Insights
1062 from low-temperature thermochronology and numerical modeling. *Journal of*
1063 *Geophysical Research: Solid Earth*, 116(5), 1–22.
1064 <https://doi.org/10.1029/2010JB007893>
- 1065 Roperch, P., Sempere, T., Macedo, O., Arriagada, C., Fornari, M., Tapia, C., et al. (2006).
1066 Counterclockwise rotation of late Eocene-Oligocene fore-arc deposits in southern Peru
1067 and its significance for oroclinal bending in the central Andes. *Tectonics*, 25(3).
1068 <https://doi.org/10.1029/2005TC001882>
- 1069 Royden, L. H., Burchfiel, B. C., King, R. W., Wang, E., Chen, Z., Shen, F., & Liu, Y. (1997).
1070 Surface deformation and lower crustal flow in eastern Tibet. *Science*, 276(5313), 788–
1071 790. <https://doi.org/10.1126/science.276.5313.788>
- 1072 Ruiz, G. M. H., Carlotto, V., Van Heiningen, P. V., & Andriessen, P. A. M. (2009). Steady-
1073 state exhumation pattern in the Central Andes – SE Peru. *Geological Society, London,*
1074 *Special Publications*, 324(1), 307–316. <https://doi.org/10.1144/SP324.20>
- 1075 Sambridge, M. (1999). Geophysical inversion with a neighbourhood algorithm –II.
1076 Appraising the ensemble. *Geophys. J. Int.*, 138, 727–746.
- 1077 Sambridge, Malcolm. (1999). Geophysical inversion with a neighbourhood algorithm - I.
1078 Searching a parameter space. *Geophysical Journal International*, 138(2), 479–494.
1079 <https://doi.org/10.1046/j.1365-246X.1999.00876.x>
- 1080 Schneider, D. A., Edwards, M. A., Kidd, W. S. F., Asif Khan, M., Seeber, L., & Zeitler, P. K.
1081 (1999). Tectonics of Nanga Parbat, western Himalaya: Synkinematic plutonism within

- 1082 the doubly vergent shear zones of a crustal-scale pop-up structure. *Geology*, 27(11),
1083 999–1002. [https://doi.org/10.1130/0091-7613\(1999\)027<0999:TONPWH>2.3.CO;2](https://doi.org/10.1130/0091-7613(1999)027<0999:TONPWH>2.3.CO;2)
- 1084 Schwarz, G. E. (1978). Estimating the dimension of a model. *Annu. Stat.*, 6, 461–464.
- 1085 Sébrier, M., Mercier, L., Francois, M., Laubacher, G., & Carey-Gailhardis, E. (1985).
1086 Quaternary Normal and Reverse Faulting and the State of Stress in the Central Andes of
1087 South Peru. *Tectonics*, 4(7), 739–780.
- 1088 Seeber, L., & Pêcher, A. (1998). Strain partitioning along the Himalayan arc and the Nanga
1089 Parbat antiform. *Geology*, 26(9), 791–794. [https://doi.org/10.1130/0091-7613\(1998\)026<0791:SPATHA>2.3.CO;2](https://doi.org/10.1130/0091-7613(1998)026<0791:SPATHA>2.3.CO;2)
- 1090
- 1091 Sempere, T., Carlier, G., Soler, P., Fornari, M., Carlotto, V., Jacay, J., et al. (2002). Late
1092 Permian-Middle Jurassic lithospheric thinning in Peru and Bolivia, and its bearing on
1093 Andean-age tectonics. *Tectonophysics*, 345(1–4), 153–181.
1094 [https://doi.org/10.1016/S0040-1951\(01\)00211-6](https://doi.org/10.1016/S0040-1951(01)00211-6)
- 1095 Shuster, D. L., Flowers, R. M., & Farley, K. A. (2006). The influence of natural radiation
1096 damage on helium diffusion kinetics in apatite. *Earth and Planetary Science Letters*,
1097 249(3–4), 148–161. <https://doi.org/10.1016/j.epsl.2006.07.028>
- 1098 Sobolev, S. V., & Babeyko, A. Y. (2005). What drives orogeny in the Andes? *Geology*,
1099 33(8), 617–620. <https://doi.org/10.1130/G21557.1>
- 1100 Springer, M. (1999). Interpretation of heat-flow density in the Central Andes. In
1101 *Tectonophysics* (Vol. 306, pp. 377–395). [https://doi.org/10.1016/S0040-1951\(99\)00067-](https://doi.org/10.1016/S0040-1951(99)00067-0)
1102 0
- 1103 Strecker, M. R., Alonso, R. N., Bookhagen, B., Carrapa, B., Hilley, G. E., Sobel, E. R., &
1104 Trauth, M. H. (2007). Tectonics and Climate of the Southern Central Andes. *Annual*
1105 *Review of Earth and Planetary Sciences*, 35(1), 747–787.
1106 <https://doi.org/10.1146/annurev.earth.35.031306.140158>

- 1107 Stüwe, K., White, L., & Brown, R. (1994). The influence of eroding topography on steady-
1108 state isotherms. Application to fission track analysis. *Earth and Planetary Science*
1109 *Letters*, 124, 63–74.
- 1110 Suarez, G., Molnar, P., & Burchfiel, B. C. (1983). Seismicity, fault plane solutions, depth of
1111 faulting, and active tectonics of the Andes of Peru, Ecuador, and southern Colombia.
1112 *Journal of Geophysical Research*, 88(B12), 10403–10428.
1113 <https://doi.org/10.1029/JB088iB12p10403>
- 1114 Sundell, K. E., Saylor, J. E., Lapen, T. J., & Horton, B. K. (2019). Implications of variable
1115 late Cenozoic surface uplift across the Peruvian central Andes. *Scientific Reports*, 9(1),
1116 1–12. <https://doi.org/10.1038/s41598-019-41257-3>
- 1117 Tassara, A. (2005). Interaction between the Nazca and South American plates and formation
1118 of the Altiplano-Puna plateau: Review of a flexural analysis along the Andean margin
1119 (15°–34°S). *Tectonophysics*, 399(1-4 SPEC. ISS.), 39–57.
1120 <https://doi.org/10.1016/j.tecto.2004.12.014>
- 1121 Valla, P. G., Van Der Beek, P. A., Shuster, D. L., Braun, J., Herman, F., Tassan-Got, L., &
1122 Gautheron, C. (2012). Late Neogene exhumation and relief development of the Aar and
1123 Aiguilles Rouges massifs (Swiss Alps) from low-temperature thermochronology
1124 modeling and $4\text{He}/3\text{He}$ thermochronometry. *Journal of Geophysical Research: Earth*
1125 *Surface*, 117(1), 1–23. <https://doi.org/10.1029/2011JF002043>
- 1126 Villegas-Lanza, J., Chlieh, M., Cavalié, O., Tavera, H., Baby, P., Chire-Chira, J., & Nocquet,
1127 J.-M. (2016). Active tectonics of Peru: Heterogeneous interseismic coupling along the
1128 Nazca megathrust, rigid motion of the Peruvian Sliver, and Subandean shortening
1129 accommodation. *Journal of Geophysical Research: Solid Earth*, 121, 7371–7394.
1130 <https://doi.org/10.1002/2015JB012608>.Received
- 1131 Whipple, K. X., & Meade, B. J. (2004). Controls on the strength of coupling among climate,

- 1132 erosion, and deformation in two-sided, frictional orogenic wedges at steady state.
1133 *Journal of Geophysical Research: Earth Surface*, 109(F1), 1–24.
1134 <https://doi.org/10.1029/2003jf000019>
- 1135 Whittington, A. G., Hofmeister, A. M., & Nabelek, P. I. (2009). Temperature-dependent
1136 thermal diffusivity of the Earth's crust and implications for magmatism. *Nature*,
1137 458(7236), 319–321. <https://doi.org/10.1038/nature07818>
- 1138 Willett, S., Beaumont, C., & Fullsack, P. (1993). Mechanical model for the tectonics of
1139 doubly vergent compressional orogens. *Geology*, 21(4), 371–374.
1140 [https://doi.org/10.1130/0091-7613\(1993\)021<0371:MMFTTO>2.3.CO;2](https://doi.org/10.1130/0091-7613(1993)021<0371:MMFTTO>2.3.CO;2)
- 1141 Wimpenny, S., Copley, A., Benavente, C., & Aguirre, E. (2018). Extension and Dynamics of
1142 the Andes Inferred From the 2016 Parina (Huarichancara) Earthquake. *Journal of*
1143 *Geophysical Research: Solid Earth*, 123(9), 8198–8228.
1144 <https://doi.org/10.1029/2018JB015588>
- 1145 Yang, R., Fellin, M. G., Herman, F., Willett, S. D., Wang, W., & Maden, C. (2016). Spatial
1146 and temporal pattern of erosion in the Three Rivers Region, southeastern Tibet. *Earth*
1147 *and Planetary Science Letters*, 433, 10–20. <https://doi.org/10.1016/j.epsl.2015.10.032>
- 1148 Zeitler, P. K., Meltzer, A. S., Koons, P. O., Craw, D., Hallet, B., Chamberlain, C. P., et al.
1149 (2001). Erosion, Himalayan Geodynamics, and the Geomorphology of Metamorphism.
1150 *GSA Today*, 11(January), 4–9.
1151